

# Search for high-amplitude $\delta$ Scuti and RR Lyrae stars in Sloan Digital Sky Survey Stripe 82 using principal component analysis

M. Süveges,<sup>1,2\*</sup> B. Sesar,<sup>3</sup> M. Váradi,<sup>2</sup> N. Mowlavi,<sup>1,2</sup> A. C. Becker,<sup>4</sup> Ž. Ivezić,<sup>4</sup>  
M. Beck,<sup>1,2</sup> K. Nienartowicz,<sup>1,2</sup> L. Rimoldini,<sup>1,2</sup> P. Dubath,<sup>1,2</sup> P. Bartholdi<sup>2</sup>  
and L. Eyer<sup>2</sup>

<sup>1</sup>ISDC Data Centre for Astrophysics, University of Geneva, Chemin d'Ecogia 16, CH-1290 Versoix, Switzerland

<sup>2</sup>Department of Astronomy, University of Geneva, Chemin des Maillettes 51, CH-1290 Sauverny, Switzerland

<sup>3</sup>Division of Physics, Mathematics and Astronomy, California Institute of Technology, Pasadena, CA 91125, USA

<sup>4</sup>Department of Astronomy, University of Washington, PO Box 351580, Seattle, WA 98195-1580, USA

Accepted 2012 May 2. Received 2012 April 27; in original form 2012 February 14

## ABSTRACT

We propose a robust principal component analysis framework for the exploitation of multiband photometric measurements in large surveys. Period search results are improved using the time-series of the first principal component due to its optimized signal-to-noise ratio. The presence of correlated excess variations in the multivariate time-series enables the detection of weaker variability. Furthermore, the direction of the largest variance differs for certain types of variable stars. This can be used as an efficient attribute for classification. The application of the method to a subsample of Sloan Digital Sky Survey Stripe 82 data yielded 132 high-amplitude  $\delta$  Scuti variables. We also found 129 new RR Lyrae variables, complementary to the catalogue of Sesar et al., extending the halo area mapped by Stripe 82 RR Lyrae stars towards the Galactic bulge. The sample also comprises 25 multiperiodic or Blazhko RR Lyrae stars.

**Key words:** methods: data analysis – methods: statistical – surveys – stars: variables:  $\delta$  Scuti – stars: variables: RR Lyrae.

## 1 INTRODUCTION

During the last decade, wide-area and multiepoch surveys have started to play a major role in astronomical research. Developments in astronomical instrumentation and in space observation techniques, together with the rapidly growing data storage facilities and the broadly available software for combining these data, provide an enormous wealth of information. The traditional manual procedures must be replaced by quick automated methods for preprocessing, selection and analysis.

Analysis of variable stars has benefited greatly from data collected by large-scale surveys such as ASAS (Pojmanski 2002, 2003), OGLE (Udalski, Kubiak & Szymanski 1997), MACHO (Alcock et al. 1997) or EROS (Aubourg et al. 1993; Spano et al. 2011). Studies of different, sometimes rare classes of objects become possible with unprecedentedly large sets of objects. These studies require specific preprocessing: a preliminary classification of the observed objects, in order to enable an efficient extraction of homogeneous samples. The first step in this procedure is variability detection, providing a set of candidate variable stars. The next is

characterization of the observed time-series by the calculation of some numerical summaries of the observed time-series. These are usually statistical moments (e.g. mean magnitude, skewness, kurtosis), derived quantities from period search (e.g. amplitudes and relative phases of harmonic components), and some astrophysical parameters such as colours. These parameters, generally called attributes in the context of classification, are then used to estimate the types of the objects. The volume of data requires fast automated data mining techniques like, for instance, those proposed by Eyer & Blake (2002, 2005). Most recently, Random Forest (Breiman 2001; Dubath et al. 2011; Richards et al. 2011; Rimoldini et al. 2012), multistage Bayesian networks (Debosscher et al. 2007; Sarro et al. 2009) and gradient boosting methods (Richards et al. 2011) were tested for this purpose with promising results.

Unfortunately, automatically distributed class labels can be less reliable than the results of a careful human inspection. A more efficient use of the information contained in the data can improve on this. The goal of this study is to consider a new way of including colour information into automated classification procedures. Although variable stars with different origin of variability and different physical parameters show different amplitudes and light-curve patterns depending on wavelength during their cycle, this variation is not easy to summarize in a concise numerical form, as it is a

\*E-mail: Maria.Suveges@unige.ch

function of phase. We attempt to find summaries of these colour variations, and to use it as complementary information to the usual attributes in automated classification of multiband survey data.

Principal component analysis (PCA, Jolliffe 2002; Hastie, Tibshirani & Friedman 2009), when applied to the quasi-simultaneous raw multiband observations, gives precisely such summaries. Its variants have already been applied in many astronomical studies in different contexts, for example, by Kanbur & Mariani (2004), Tanvir et al. (2005), Yoachim et al. (2009), Deb & Singh (2009), Savanov & Strassmeier (2008) or Paltani & Türlér (2003). Our methodology, different from these, considers the vector of raw observations in  $M$  bands at one time as a point in an  $M$ -dimensional space, and looks for a decomposition of the space of observations into directions with maximal variance. The first direction is called the first principal component or PC1. The projection of any point in the PC1 direction is a linear combination of the simultaneous measurements with constant coefficients, which is called PC1 score. It provides several potential advantages. It improves signal-to-noise ratio when searching for periods on the time-series of the projections in the direction of PC1. It yields a variability criterion based on the presence of correlated variations across filters. Also, the direction of PC1 is characteristic to the origin of variability and to the physical properties of the star, and is useful to separate eclipsing binaries from some pulsating variables with symmetric light curves, such as RR Lyrae type c (hereafter RRC) variables. We demonstrate these advantages on five-band time-series from a flux-limited sample of Stripe 82 objects of the Sloan Digital Sky Survey (SDSS).

However, applying PCA on astronomical time-series is not straightforward. Usually, the data in different filters have different error levels, depending on the measured magnitudes too. Outliers and non-normality can also strongly influence PCA, which is built entirely on the assumption of normality. Since usually not all types of errors can be anticipated and accounted for in advance, the robustness of the methods is very desirable: a good automated method should be able to function acceptably well even in the presence of contaminations from various unknown sources. We propose a combination of variance stabilizing transformation with robust PCA to minimize the impact of these issues.

After constructing the methodology, we use it to select samples of candidate RR Lyrae and high-amplitude  $\delta$  Scuti (HADS) stars from SDSS Stripe 82. RR Lyrae stars are interesting as they are Population II halo structure tracers, and obey well-determined period–luminosity relations (e.g. Smith 1995). Stripe 82 RR Lyrae stars have been used to investigate the outer Galactic structures by Watkins et al. (2009) and Sesar et al. (2010), resulting in the identification of clumps in their distribution and thus suggesting new structural elements of the Galactic halo. The HADS stars are pulsating variable stars with spectral type from late A to early F, occurring in the instability strip on and just above the main sequence below the RR Lyrae stars (e.g. Breger 1980; McNamara 2000b; Clement et al. 2001; Pigulski et al. 2006). Their pulsation is in majority radial mode, though for some, there are indications of non-radial modes (Mazur, Krzemiński & Thompson 2003; Poretti 2003). Metal-rich Population I ( $\delta$  Scuti) and metal-poor Population II (SX Phoenicis) objects are mixed in the group, and thus their further distinction requires estimation of metallicity. They also satisfy period–luminosity relations depending on metallicity and oscillation mode (Nemec, Nemec & Lutz 1994; McNamara 1995, 1997, 2000a,b). In Stripe 82 data, the confirmed RR Lyrae stars published by Sesar et al. (2010) will be used as a performance test and a training set for the PCA-based methodology. For HADS stars, we build a training set to obtain a clean sample in Stripe 82. Finally,

we present a list of 129 new RR Lyrae and 132 HADS candidate variables.

In Section 2, we briefly present SDSS Stripe 82 (York et al. 2000). Section 3 summarizes the statistical background: variance stabilizing transformation and PCA with its robust version, the tested period search variants, and the Random Forest classifier. Section 4 describes the results obtained by PCA in variability detection, period search, characterization and classification. A short summary and a discussion follow in Section 5. All analyses in this paper were done using the R statistical software and its packages MASS, RRCOV, MVTNORM, RANDOMFOREST, EVIR and EVD (R Development Core Team 2010).

## 2 SDSS STRIPE 82

SDSS provides five-band ( $u$ ,  $g$ ,  $r$ ,  $i$  and  $z$ ) photometry of more than 11 000 deg<sup>2</sup> of the sky (for Data Release 7 which provides the most extensive catalogue of Stripe 82, see Abazajian et al. 2009). The photometric errors are around 0.02 mag for  $g < 16$  mag, and around 0.04 mag for  $g \sim 21$  mag (see fig. 2 of Sesar et al. 2010). Equivalent values for the noisiest  $u$  band are 0.02 mag at the bright end and 0.05 mag around 20 mag. The 95 per cent completeness limits of the images are  $u = 22.0$ ,  $g = 22.2$ ,  $r = 22.2$ ,  $i = 21.3$ ,  $z = 20.5$  (Abazajian et al. 2004). One of the southern regions, Stripe 82, was observed repeatedly during the first phase of SDSS (SDSS-I) and the following SDSS-II Supernova Survey (Bramich et al. 2008; Frieman et al. 2008). The median time-span for time-series consisting of at least 10 complete  $ugriz$  observations is around 9 yr (with the mean around 7.3 yr). The measurements in the five bands were taken quasi-simultaneously, with around 1.2 min time-difference between band records.

Our data set is a flux-limited subset of Sesar et al. (2007), separated into around 68 000 variable and 200 000 non-variable objects with the median  $g$  magnitude brighter than 20.5 mag (the catalogue can be downloaded from <http://www.astro.washington.edu/users/ivezic/sdss/catalogs/S82variables.html>). The variable flag used there was based on two criteria: (1) for the root-mean-square scatter in  $g$  and  $r$ ,  $\sigma_r > 0.05$  and  $\sigma_g > 0.05$ , respectively; and (2) for the reduced chi-square in  $r$  and  $g$ ,  $\xi_r \geq 3$  and  $\xi_g \geq 3$ , respectively. This selection will be referred to as ‘flagged as variable’ or ‘flagged as non-variable’ hereafter, and will serve in comparisons with the PCA-based detection method. Details about the construction and testing of the catalogue are described in Ivezić et al. (2007). Sesar et al. (2010) published 483 confirmed RR Lyrae variables in Stripe 82; our subset of data contains 450 of these. The loss of 33 objects is due to the cut on the median  $g$ -band magnitude in the used catalogue. The existence of a confirmed variable sample makes Stripe 82 data particularly adapted to test our methods, as we can check their performance by direct comparison to previous analyses of a largely overlapping data set.

## 3 STATISTICAL TOOLS

### 3.1 Principal component analysis

PCA is a statistical tool developed for finding orthogonal directions of maximal variance in high-dimensional data sets. It is assumed that directions of large variance are of particular interest: in signal processing, they may contain the bulk of the information transmitted by a signal; in image analysis, they may concisely summarize the most characteristic pattern forms; or in classification, they might coincide with the directions that best separate some distinct groups

of objects. In order to find them, we consider the point cloud of multifilter observations plotted against each other, regardless of times. The goal is to find an orthogonal coordinate system adapted to this point cloud: the first axis is fixed so that it points to the direction of maximal variance. Next, the points are decomposed into projections to this first axis and to its orthogonal subspace. Then the second axis is chosen to point into the direction of largest variance in the orthogonal subspace. These steps are repeated until an orthogonal basis spanning the original space is found. Mathematically, we seek for a successive decomposition of the space of the observables into orthogonal directions to which the projections of the points have the highest residual variance.

Suppose that we observed  $M$  sequences  $X_{11}, X_{21}, \dots, X_{N1}, \dots; X_{1M}, X_{2M}, \dots, X_{NM}$  at  $N$  times, with the values  $X_{i1}, X_{i2}, \dots, X_{iM}$  observed simultaneously. This corresponds to a sequence of observations made in an  $M$ -dimensional space, where a joint observation  $X_{i1}, X_{i2}, \dots, X_{iM}$  is represented by a point in the  $M$ -dimensional state space. If we define the matrix  $\mathbf{X}$  so that its columns are the  $M$  sequences, and the rows correspond to the different  $M$ -dimensional observations, then we can write the sample covariance matrix as  $\mathbf{X}^T \mathbf{X} / N$ , with the superscript ‘ $T$ ’ denoting transposition. Finding orthogonal directions of maximal variance turns out to be equivalent to finding the eigendecomposition

$$\mathbf{X}^T \mathbf{X} = \mathbf{V} \mathbf{D}^2 \mathbf{V}^T.$$

Here the columns of  $\mathbf{V}$  are the eigenvectors or, in other terms, the principal directions of  $\mathbf{X}$ , and  $\mathbf{D}^2$  is a diagonal matrix with non-negative values  $d_1^2, d_2^2, \dots, d_M^2$ , representing the variances of the projections of the points on the principal directions. By convention, the order of the directions is such that  $d_1^2 > d_2^2 > \dots > d_M^2$ , and therefore the first principal component corresponds to the direction of the maximal variation. The vector of projections of the points on the first principal direction can be written as the linear combination  $\mathbf{z}_1 = \mathbf{X} \mathbf{v}_1$ , where  $\mathbf{v}_1$  is the first column of the matrix  $\mathbf{V}$ .

How to apply this for variable star analysis? For  $M$  time-series of a star consisting of  $N$  simultaneously taken points, we consider the  $M$ -dimensional point cloud of the observations, as shown in Fig. 1. We intend to apply PCA in order to find the direction where variability is maximal, so that we can find more easily the period of the variable star. However, the application immediately hits an obstacle visible in Fig. 1, the different average noise in the different bands. Even if a star shows coherent deterministic variations across the bands, this can be easily masked by the noise in one of the bands (in SDSS, the noisiest bands are generally the  $u$  and  $z$  bands). PCA will pick the direction of the noisiest band as shown by the blue ellipsoids in the upper middle and right-hand panels of Fig. 1, and not the direction of coherent variations. The remedy is to use the estimated errors to scale the observations so that we have unit variance in every band. In the case of a non-variable star and near-independent errors, this implies that the point cloud appears as a sphere. For a variable star, the noise is added to a deterministically varying light curve, which causes the centre of the sphere to move in the  $M$ -dimensional space, and instead of a ball, we observe an elongated ellipsoid-like shape. The first principal direction is the longest axis of this shape, providing the largest variability amplitude that can be obtained by a linear transformation.

Assume that the distribution of the observations is  $X_{im} \sim \mathcal{N}(\mu_m, \sigma_{im}^2)$ , that is, the star is constant with mean magnitude  $\mu_m$  in band  $m$ , the standard deviation of the measurement  $X_{im}$  around the mean is  $\sigma_{im}$ , and the error distribution is normal. We have several options to obtain unit variance of the noise.

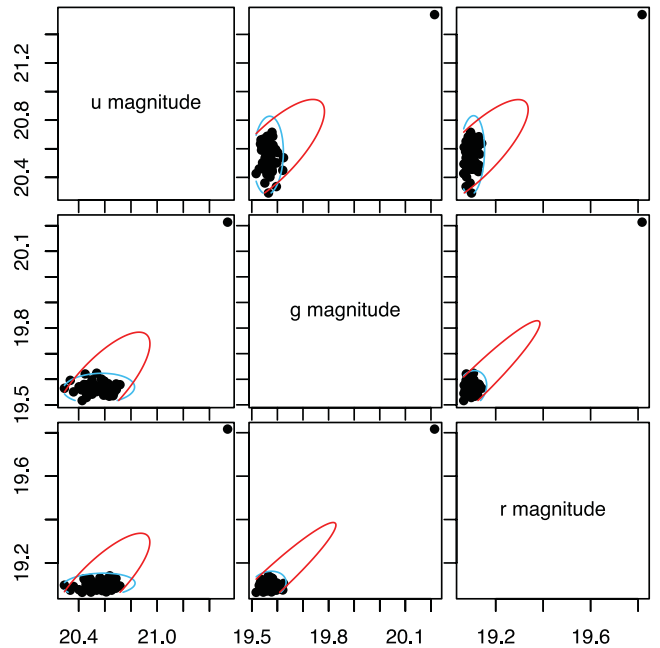


**Figure 1.**  $u$ ,  $g$  and  $r$  magnitudes of a randomly chosen star flagged as variable from SDSS Stripe 82. The red ellipsoids are levels of equal probability density fitted by non-robust maximum likelihood and the blue ones are the same levels from a robust fit by the minimum covariance determinant method.

(i) We can centre and scale the measurements by an estimate of the centre and the pointwise error estimates (called here local scaling):

$$Y_{im} = \frac{X_{im} - \hat{\mu}_m}{\sigma_{im}} \quad \text{for all } m = 1, \dots, M,$$

where  $\hat{\mu}_m$  can be either the mean or the median of  $X_{im}$ .

(ii) We can centre and scale the measurements by an estimate of the centre and the square root of the average variance of the time-series:

$$Y_{im} = \frac{X_{im} - \hat{\mu}_m}{\hat{\sigma}_m} \quad \text{for all } m = 1, \dots, M,$$

where  $\hat{\mu}_m$  and  $\hat{\sigma}_m^2$  can be either the mean (non-robust scaling) or the median (robust scaling) of  $X_{im}$  and  $\sigma_{im}^2$ , respectively. In the case of correlated errors that can be assumed normal, an analogous matrix transformation can be based on the covariance matrix. In this paper, we assume that the correlation between the errors is weak compared to the correlation between bands for an RR Lyrae or HADS star (Scranton et al. 2005).

(iii) Considering that the errors depend on true magnitudes, and this effect can be strong for some classes of variable stars or very faint objects, we tested also the variance stabilizing transformation (Everitt 2002). Suppose we have a random variable  $X$  from a distribution with mean  $\mu$  and variance  $\sigma^2$  for which  $\sigma^2 = g(\mu)$ . Define the function  $f$  as the solution to  $f'(x) = [g(x)]^{-1/2}$ . Then the transformation  $Y = f(X)$  leads to a variable with unit variance:  $\text{Var}(Y) = 1$ . In our case, we supposed a functional form  $\sigma^2 = g(x) = a \exp(bx)$  between the variances  $\sigma_{im}^2$  and centred observed magnitudes  $x_{im}$  with different coefficients for each band. This corresponds to a rough approximation with Poisson noise, which leads to an easily tractable closed-form transformation. Fitting this function bandwise to observed magnitudes and squared standard errors of a sample of variable and non-variable stars resulted in the bandwise estimates

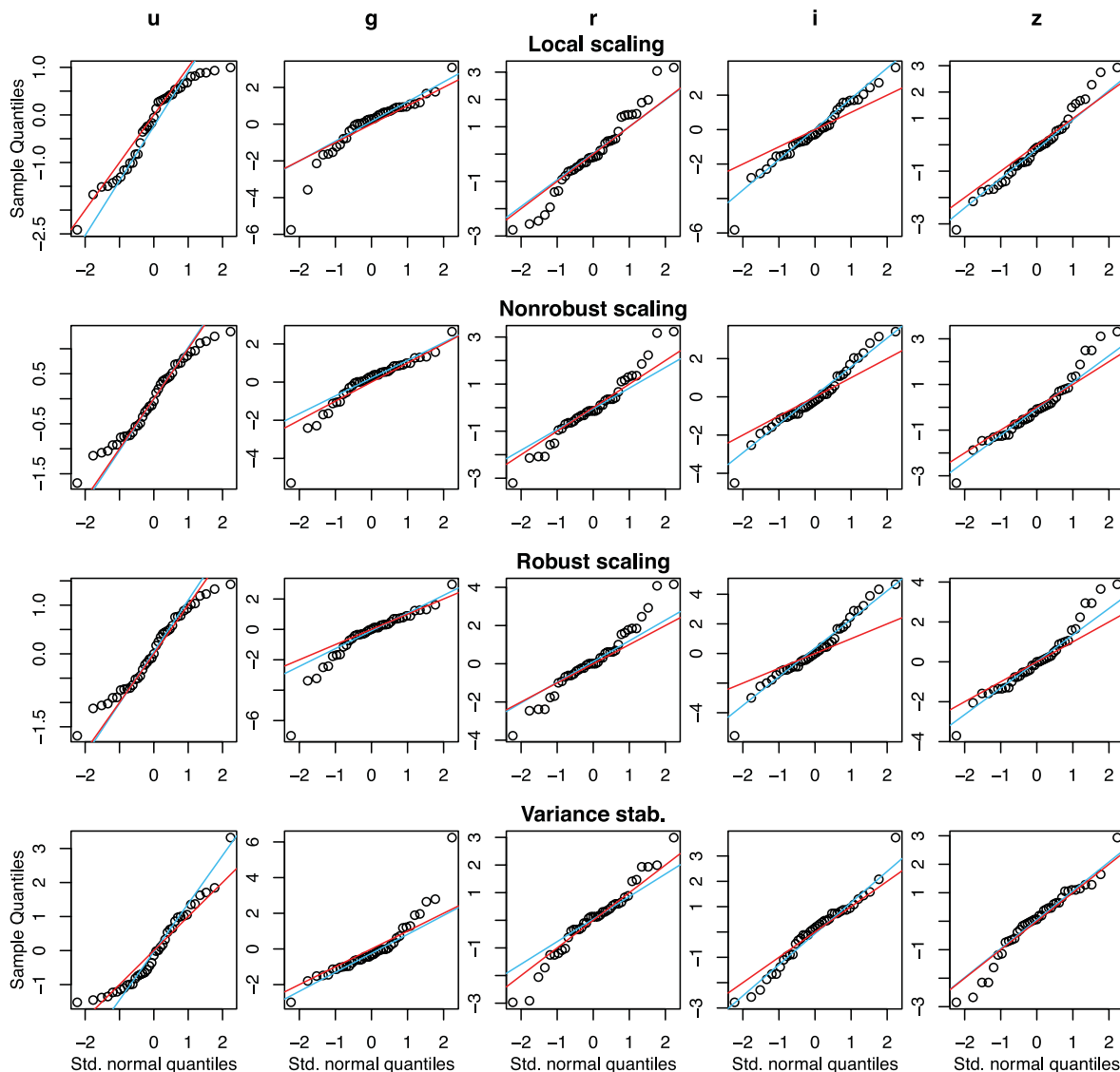


**Figure 2.** Q–Q plots of a non-variable star from Stripe 82. The columns are the five bands  $u, g, r, i, z$ . The rows correspond to different scaling methods: (from the top) first row – local scaling; second row – non-robust scaling; third row – robust scaling; fourth row – variance stabilizing transformation. The red line corresponds to a standard normal distribution and the blue line to a robustly fitted best-fitting normal distribution to the data.

$\hat{a}_m$  and  $\hat{b}_m$  and a transformation  $Y_{im} = 2\hat{a}_m^{-1/2}\hat{b}_m^{-1}\exp(-\hat{b}_m x_{im}/2)$  for band  $m$ . Then the point cloud of  $Y_{im}$  is centred by removing either the mean or the median from it.

The assumption of normality can be checked by quantile–quantile (Q–Q) plots (Chambers et al. 1983; Cleveland 1994). After scaling and centring, the ordered sample of transformed magnitudes of a star is plotted against the corresponding theoretical quantiles of the standard normal distribution. If the sample follows indeed the standard normal distribution, then the points should be aligned along a straight line with intersect 0 and slope 1. If the assumption of normality is true, but the mean and the variance are not 0 and 1, the points still fit on a straight line, but the intersect and the slope of the line change to the mean and the standard deviation, respectively. If even normality is not satisfied, the points deviate systematically from the straight line. Fig. 2 shows the Q–Q plots of a constant star for all variants of scaling, with the expected standard normal line pictured in red, and the best-fitting normal distribution in blue.

The sample is visibly not normal in any of the bands: the tails deviate from both lines, indicating heavier tails (the absolute values of the observations are larger than what is expected from a normal distribution). The blue and the red lines have only slightly different slopes in most of the plots, suggesting that the scaling did obtain approximately unit variance, though the assumption of normality is not valid.

This implies that the non-robust PCA, built on the assumption of normality, is not appropriate for our purposes. Another important issue that violates this distributional condition is the presence of outliers. We can see their effect in Fig. 1: a single outlier distorts completely the estimated normal distribution, outlined by the red ellipsoid. Robust versions of PCA are given in the statistical literature, among which we chose the minimum covariance determinant method (Rousseeuw 1985). This involves repeated random subsampling of the data, leaving out a fixed per cent of the observations each time. Then the covariance matrix is computed using each subsample, and the one having minimal determinant is chosen



as the robust estimate. The blue ellipsoids in Fig. 1 are the result of the application of this method. The per cent of left-out data is fixed so that the effect of a single outlier is decreased, but that of a few consistently located outlying observations is preserved. This choice is motivated by two conflicting aims. One is to get rid of the effects of true erroneous observations. The other is to preserve that of those that are true representatives of the light curve, though they are rare, for instance, scarce measurements of the dips in detached eclipsing binaries. Indeed, the blue ellipsoids in Fig. 1 represent better the apparent distribution of the bulk of the data.

Robust PCA yields some directly useful quantities. The first are the coefficients  $v_1$  of the linear combination, which characterize the direction of the first principal component. It depends on the type of variability, and thus can be used in classification. The second are the scores of the observations on the first principal component, that is, the time-series of the linear combinations  $z_1 = \mathbf{X}v_1$ . By convention, the linear coefficients  $v_1$  are fixed so that the variance of the noise after transformation remains 1, so the improvement on the signal-to-noise ratio is  $\sum_{m=1}^M v_{m1} A_m$ , where  $A_m$  is the signal amplitude in band  $m$  after scaling. The third is the variance  $d_1^2$  of  $z_1$ , which is related to the elongation of the point cloud. Its ratio to the total variance  $\sum_{m=1}^M d_m^2$  (called hereafter the variance proportion) gives indication about the presence of variability. Finally, the distances of the observations from the centre with respect to the robust variance-covariance matrix fit indicate outlyingness of the observations, and can be used to weight the observations in period search.

### 3.2 Period search

We used the generalized Lomb–Scargle method (Zechmeister & Kürster 2009) to obtain the periodogram of the first principal component, and tested various trimming and weighting options on simulated sinusoids with errors imitating SDSS error patterns.

The usual weighting with the inverse-squared errors cannot be applied for the  $z_1$  time-series, because the scaling and the construction of the principal components lead to approximate unit variance of the noise on  $z_1$ . Instead, we can base a measure of outlyingness on the robust distances, and trim or weight the elements of the time-series according to this measure. The squared distances,  $r_i^2$ , in an  $M$ -dimensional space under the hypothesis of approximate standard normality should follow a  $\chi_M^2$  distribution. Similarly to the principle of Q–Q plots, we can determine what value is expected for the  $i$ th largest distance,  $r_{(i)}^2$ , among a sample of size  $N$  according to the  $\chi_M^2$  distribution: this will be the  $i/(N+1)$  quantile,  $c_{M,i/(N+1)}$ , of the  $\chi_M^2$  distribution ( $N+1$  is taken instead of  $N$  to avoid exactly 0 or 1 values). Such a  $\chi_5^2$  Q–Q plot of the robust distances is shown in Fig. 3 for a variable star. We checked various alternatives of trimming thresholds and weight definitions based on the difference between the  $i$ th largest observed distances and  $c_{M,i/(N+1)}$ .

The goal of the simulations is to reproduce the SDSS error levels, error dependence on magnitude, outliers and observational cadences. In order to obtain this, we followed the following procedure:

(1) From 2000 randomly selected objects from the 68 000 Stripe 82 objects flagged as variable, we extracted sets of five amplitudes based on the excess root-mean-square variability, sets of five median magnitudes and the  $u$ -band observational times.

(2) We generated 200 sine functions with random frequencies in the interval  $[0, 20] \text{ d}^{-1}$ , with random phases, and randomly selected sets of five amplitudes and median magnitudes from those extracted from our sample. Each sine function was multiplied by all five elements of one amplitude set, and one set of median magnitudes

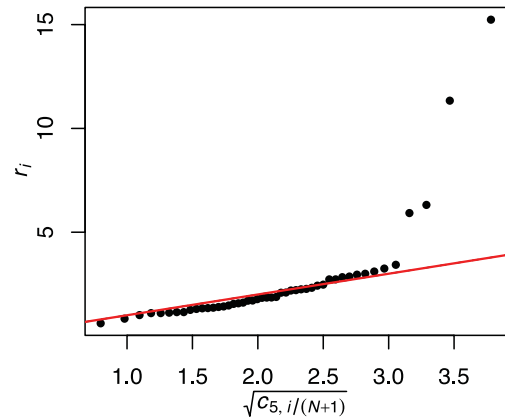


**Figure 3.** Robust distances from the centre of the point cloud for the five-dimensional observations of a star, on a square root scale for better visibility. The red line indicates the exact  $\chi_5^2$  distribution.

was added to it. We thus obtained 200 pure five-band light curves, each with coherent brightness variations in the bands. We sampled these sine waves with time cadences extracted from Stripe 82 in the previous step.

(3) We added noise to the light curves. We divided the full magnitude range of the 2000 stars in each filter into 0.5-mag-wide bins, and grouped the error bars according to the magnitude value with which it occurred. We thus obtained a sample of all error bars, in magnitude bins, for all bands. Then for each simulated magnitude value of the sinusoidal light curves in each band, we randomly selected an error bar value  $\epsilon$  from the bin corresponding to the simulated magnitude value in that band. We generated a random number from the  $\mathcal{N}(0, \epsilon^2)$  distribution, and added this value as the realized noise to the simulated magnitude. Finally, we joined  $\epsilon$  as the error bar to the simulated series.

(4) To simulate outliers, we changed some observations to fainter values. The differences were random values from  $\mathcal{N}(0, (6\epsilon)^2)$ , in a random number of filters for randomly selected epochs. The number of selected epochs followed a Poisson distribution with the mean equal to 0.005.

Visual inspection and Q–Q plots showed that the observed and simulated light curves are very similar. The simulations were then used to investigate the performance of different combinations of scaling, weighting or trimming and period search. We found that the combination leading to the highest frequency recovery rate was the generalized Lomb–Scargle method with weights defined by

$$w_i = \frac{1}{W} [\max\{1, |r_i^2 - c_{5,i/(N+1)}|\}]^{-1/2} \quad (1)$$

with  $W = \sum_{i=1}^N [\max\{1, |r_i^2 - c_{5,i/(N+1)}|\}]^{-1/2}$ , applied either to the  $z_1$  time-series derived from variance stabilized observations or to observations scaled with robust estimators of the mean and standard deviation.

For comparison, the generalized Lomb–Scargle method with the usual weights based on error bars was also applied to detect periodicity on the single  $g$  band, which generally had the best signal-to-noise ratio. The results of the best  $z_1$  and the single-band analysis are compared in Fig. 4. The logarithm of the difference between the found and the true frequency is shown versus the number of observations in the time-series. Period search on  $z_1$  outperforms the single-band analysis. While the single-band analysis finds a yearly or daily alias in 31 cases, the analysis of  $z_1$  reduces this number to only 8.

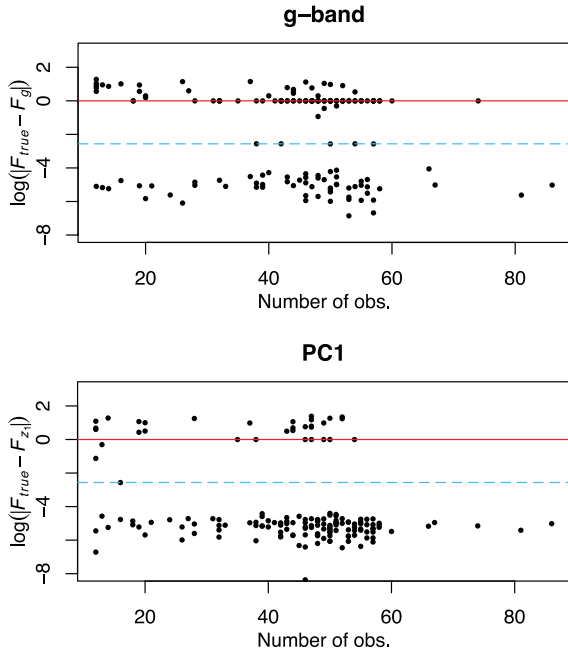


**Figure 4.** The logarithm of the difference between the true and the found frequency in  $d^{-1}$  for sinusoidal light-curve simulations with approximate SDSS error distributions on the  $g$  band (top panel) and on PC1 (bottom panel). The solid red and dashed blue lines are the daily and the yearly aliases, respectively.

Based on these simulation results, in the analysis of the variable stars in Stripe 82 we applied the generalized Lomb–Scargle method with weights defined by equation (1). For some variable stars, we also performed a multifrequency analysis. The folded  $z_1$  light curves were fitted with B splines, restricting the smoothing parameter to provide a reasonable degree of smoothing (R procedure `smooth.spline` with the constraint  $0.5 \leq \text{spar} \leq 1$ ; R Development Core Team 2010), and selecting its optimal value by leave-one-out cross-validation. The smoothed light curves  $\hat{z}_1$  were inspected visually, and the rare over- or under-smoothed cases were corrected by a manual selection of the smoothing parameter. The frequency analysis of the residuals was not performed on light curves where the equivalent degree of freedom of the smoothing was high with respect to the number of data points, since this left too few residual degrees of freedom to obtain meaningful harmonic fits in the residual frequency spectrum. For the cases with enough residual degrees of freedom, the residuals  $\mathbf{r} = \mathbf{z}_1 - \hat{\mathbf{z}}_1$  were extracted from the B-spline model, and the same period search algorithm with the same weights as for  $\mathbf{z}_1$  was performed on their time-series. The significance of eventual peaks in the residual periodogram was assessed using a combination of non-parametric bootstrap (Davison & Hinkley 2009) and extreme-value methods (Coles 2001).

### 3.3 Random Forest

Supervised classification methods estimate the class (usually a discrete variable like 1, 2, ...,  $L$  or RRAB, RRC, EA, EB, ...) for an object of unknown class based on some attributes (e.g. period, amplitude, colour, etc.), by fitting a model to a set of objects with measured attributes and known classes (the training set), and then using this for prediction. Random Forest (Breiman 2001; Hastie et al. 2009) is a popular method which works excellently in a very wide range of data mining problems. It consists of building a collec-

tion (‘forest’) of classification trees on the training set, then passing any new instance down on all trees and obtaining the class estimate by the majority vote of the forest.

The training (‘growing of the forest’) begins with a selection of a large number of bootstrap samples from the training set. Then a classification tree is built separately for each sample with binary splits. First, a relatively small subset of attributes are selected randomly. For each of these, the split point is computed which separates the given bootstrap sample with the least mixing of classes by some criterion (e.g. one of the subsets contains only classes A and B, whereas the other mostly C and D). Then the tree is split according to the attribute for which this separation is the cleanest. For the next step, both subsets (called nodes) are further split in the same way as was done in the first step: from a small random subset of attributes, the one that splits best the node in question is selected. The procedure is repeated until each final node is either perfectly clean or has a predefined minimal size. Then, using another bootstrap sample from the training set, a new tree is built. As a result, a large forest of many trees emerge. To classify a new object, the prediction of the class by each tree in the forest is computed, and the class that is predicted by the largest number of trees is accepted as the estimate. An estimate of the probabilities to belong to each of the classes can also be obtained by calculating the proportion of votes for each class.

The main advantage of this procedure is that it obtains the class estimate as an average of many individual estimates by the trees. These estimates are unbiased, but have high variance. Averaging preserves unbiasedness and reduces variance, and this variance reduction is larger, if the trees are less correlated (Hastie et al. 2009). Random Forest achieves decorrelation by applying two tricks: first, it uses only bootstrap samples from the training sets, so the basic data set driving the learning process is not identical for each tree; and secondly, it uses the best of only a random subset of attributes, not of all attributes. The consequent higher variance of the individual trees is more than compensated by the decrease of the variance of the average because of the nearly non-correlated trees.

There are a few tuning parameters in the Random Forest procedure: the number of trees in the forest, the number of random attributes at the nodes, and the final node size. For most classification problems, growing several hundred trees is enough, and adding more trees does not improve the prediction accuracy. With respect to the final node size, optimal results are achieved by maximally growing the trees (i.e. the minimal final node size is 1), but it is customary in larger problems with many instances and attributes to grow the trees only to a somewhat larger final node size to speed up the process without great loss of accuracy. The most influential tuning parameter is in general the number of attributes from which the best split is chosen at the nodes, though Random Forest is only weakly sensitive to this as well. Breiman (2001) proposes to choose the largest integer  $k$  such that  $k < \sqrt{K}$ , where  $K$  is the number of attributes.

## 4 APPLICATION TO DATA

### 4.1 Principal component analysis

We considered only stars that have at least 10 complete *ugriz* observations from our data set. As discussed in Section 3.1, scaling and centring are necessary before applying robust PCA. We tested all four methods (local scaling, robust and non-robust average scaling, and variance stabilization) outlined there for variability detection, characterization and period search. The requirements of these three

tasks are not the same, and thus different scaling methods perform better in each one, but inspection of the results suggested that variance stabilization yields the best overall performance. We present here only the results based on this transformation.

#### 4.1.1 Variability detection based on $z_1$ variance

After scaling and centring the data, we expect to see a spherical point cloud, similar to a multivariate standard normal sample, if the errors are nearly non-correlated and the star is constant. Detection of variability is thus equivalent to detecting excess variance in the point cloud of the scaled observations as compared to the variance of the first principal component of a five-dimensional standard normal point cloud. Samples from even a spherically symmetric distribution show stochastic distortions from the perfect sphere, and the smaller the number  $N$  of the points in the cloud is, the stronger this distortion is. As PCA selects the direction of maximal spread in the data, we cannot expect  $d_1^2$  to be exactly 1. The distribution of  $d_1^2$  as a function of  $N$  is the easiest to obtain with simulations. The zero hypothesis of non-variability of a source may be tested at a given confidence level  $\alpha$  by comparing the observed  $d_1^2$  of the source to the quantile  $c_{1-\alpha}$  of the simulated distribution:  $d_1^2 > c_{1-\alpha}$  rejects the hypothesis of non-variability of the source at the level  $\alpha$ .

As a PCA-based selection criterion, we use the proportion of  $d_1^2$  to the total variance. Fig. 5 shows its comparison to the variable selection of Sesar et al. (2010). 500 objects that were flagged as variable (black dots) and 500 flagged as non-variable (filled grey triangles) are plotted, together with the RR Lyrae sample of Sesar et al. (2010) (empty blue circles). The 0.9999 quantile derived from the simulations is denoted by the red line. For sources that are above this line, non-variability is rejected at the level of 0.0001. The left-hand panel shows the proportion of  $d_1^2$  to the total variance. Most of the objects flagged as variable (black dots) are above the red line, meaning that the variance proportion criterion and the classical cuts select approximately the same variable sample. Some difference nevertheless can be observed. Among the stars flagged as non-variable, the PCA-based criterion found some variables: the grey triangles above the red line. The significant variance excess seems to be due to two reasons. When the bands are weakly correlated, the excess might be the consequence of either microvariability, or correlated

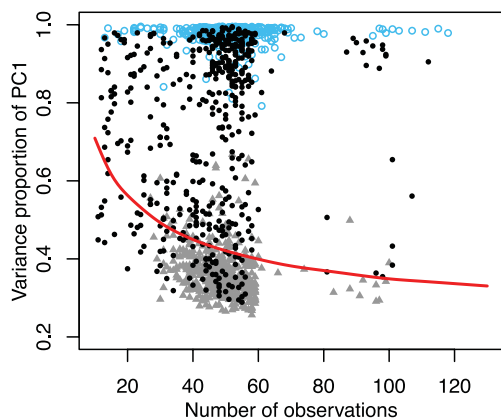


**Figure 5.** The proportion of the variance of the first principal component to the total variance versus the number of observations for the RR Lyrae sample of Sesar et al. (2010) (empty blue circles), and for 500 variable and 500 non-variable random objects (black dots and grey triangles, respectively). The 0.9999 quantiles of the simulated distributions are added as a red line.

and underestimated errors across bands (Scranton et al. 2005), so to detect microvariability in Stripe 82, a decorrelated version of scaling should be used. The other is that the variance stabilization did not succeed to obtain unit variance in one band. In this case, the point cloud is elongated along one axis. Correspondingly, the coefficients  $v_1$  of the first principal component contain usually one value close to 1 at the band which is the origin of the excess variance and a value close to 0 for all others. The characteristic profile of  $v_1$  helps to recognize these cases.

Conversely, the black dots below the red line in the left-hand panel of Fig. 5 represent points that are flagged as variable but found non-variable by PCA. These seem to belong to two groups: one for which the flag seems to originate from an outlier, and another that appears ball like on the pairwise scatterplots like Fig. 1, but not with unit variance. The variable flag from the classical analysis in the latter case can be due to underestimated but nearly non-correlated errors in all bands (Scranton et al. 2005). If the underestimation is of similar order in every band, then the PCA-based criterion is less biased than traditional cuts, as it is defined as a proportion. Moreover,  $v_1$  would again contain one value close to 1 and all the others near-zero, so it is possible to filter out these cases based on the  $v_1$  profile. In general, this form of  $v_1$  can be used to recognize and filter the cases where the excess scatter is due to underestimated errors in one or a few bands rather than true variability of the source.

#### 4.1.2 Period search on PC1 time-series

For the majority of the investigated variable objects, period search on the SDSS time-series suffers from aliasing problems. The daily and yearly observational patterns (see e.g. Sesar et al. 2007, 2010) create aliases with complex structures, displaying combinations of the variability frequency with the  $1\text{ d}^{-1}$  and  $1\text{ yr}^{-1}$  frequencies with comparable amplitudes. According to the simulation results of Section 3.2, using the time-series of  $z_1$  with weights defined by equation (1) improves on period search on the  $g$  band. We applied this procedure, complemented by a non-linear optimization, to find the exact value of the frequency, to a small random sample of 2000 stars flagged as variable, which contained 36 known RR Lyrae stars. The published periods of these RR Lyrae stars, as described in Sesar et al. (2010), were determined by a visual inspection of light curves folded with the five best periods returned by the SuperSmoother algorithm (Reimann 1994) restricted to the  $[0.2, 1]$  d interval. For 30 out of the 36 RR Lyrae stars, the result from our algorithm coincided with the true frequency. In the six other cases, daily alias periods were found. This suggests that we can expect good period search results from a simple automatic procedure even in the absence of visual inspection.

We applied the weighted period search method (without the non-linear optimization) on the full variable star set. The dominant frequency was used as an attribute in the classification procedures, presented in Section 4.2. The classification selected a sample of 317 candidate RR Lyrae and HADS stars. For these, we modelled the folded  $z_1$  light curve, computed the residuals  $r = z_1 - \hat{z}_1$ , and performed another period search on  $r$  as described in Section 3.2. The found potential multiperiod objects are discussed in Sections 4.2.2 and 4.2.3. For both PC1 and residual time-series on all candidates, we checked and, where necessary, refined frequencies using the  $F\chi^2$  procedure of Palmer (2009), which calculates the  $\chi^2$  value by fitting Fourier series including a fixed number of harmonics at each trial frequency. The found frequencies in most cases agreed with previous results within  $4 \times 10^{-5} \text{ d}^{-1}$  or, in a minority, produced daily or yearly aliases. Finally, the best

frequency was decided by a visual inspection of the light curves folded by the found best frequency and its  $-2$ ,  $-1$ ,  $+1$  and  $+2$  daily aliases.

#### 4.1.3 Characterization of variability with the PC1 spectrum

Often, variable stars with sharply different origin of variability can show very similar folded-light-curve patterns, which makes their automated classification very hard. This is the case for the distinction between contact binaries and RRc stars. Both have highly symmetric, sinusoidal light curves, and despite a period–colour relationship for contact binaries which defines a region in the attribute space for these objects (Terrell, Gross & Cooney 2012), the machine learning algorithms still produce high mixing between these two classes. A difference between them is the pattern of colour variations through the cycle.

RR Lyrae variables show a characteristic wavelength-dependent amplitude pattern: their variability is stronger at shorter optical wavelengths than at the red end of the spectrum (Smith 1995). If we could observe RR Lyrae stars with SDSS filters with equal errors in all bands, we would see the first principal direction tilted towards the blue rather than the red bands, and correspondingly, larger coefficients  $v_1$  for blue than for red wavelengths. However, the error patterns distort this simple picture. We must scale the bands in order to get rid of the effect of different average error levels, and the downscaling will be stronger in bands with larger errors, most notably in  $u$  and  $z$ . This downscaling also depends on the distance of the star: its pattern will be slightly different for a nearby and a distant object, even if they have the same amplitude vector. As a result, variability amplitudes get downscaled as well. Thus, the typical RR Lyrae  $v_1$  pattern (the PC1 spectrum) takes a characteristic shape. It is composed of, on the one hand, the amplitude pattern of pulsating variables governed by the physical parameters and pulsation mode, and, on the other hand, of the scaling patterns of the survey and the distance of the star. Typical PC1 spectra of identified R Rab and RRc stars are shown with the black lines in the middle panel of Fig. 6. They exhibit small coefficients  $v_{u1}$  and  $v_{z1}$  for the  $u$ - and  $z$ -band

contributions, and the highest value is  $v_{g1}$  at the  $g$  band, which has high variability amplitude and low errors.

HADS variables are in some aspects similar to the RR Lyrae variables (see e.g. Breger 1980; McNamara 1995; Petersen & Christensen-Dalgaard 1996; McNamara 1997; a light curve is shown in the bottom left-hand panel of Fig. 6). Their effective temperature is roughly in the same range, and although their pulsation may be more complex than that of RR Lyrae variables, they are mainly radial-mode pulsators. They show similar patterns across the wavelengths with decreasing amplitudes from blue to red wavelengths (Pigulski et al. 2006), so we can expect their PC1 spectrum to be similar to that of RR Lyrae stars. The middle panel of Fig. 6 presents the PC1 spectrum of several variables that were found to have periods, colours and folded light curves characteristic to HADS variables. These are plotted in blue, superposed on the lines of the RR Lyrae stars.

For some other types of variability, we can expect different PC1 spectra. Eclipsing binaries that are composed of two components of the same age and similar masses have similar colours, and therefore show only weak colour changes and an almost-equal contribution of all bands to the light variation. This results in a flatter PC1 spectrum. Combined with the specific error pattern of SDSS, this yields a profile that is low at the noisy  $u$  and  $z$  bands and has a higher plateau at  $g$ ,  $r$  and  $i$ . Several PC1 spectra of this type are also shown in the middle panel of Fig. 6; these objects have clear eclipsing binary-type folded light curves.

Fig. 6 shows the use of the PC1 spectrum for discriminating certain types. In the two panels on the right-hand side, we show the light curve of an RRc star from the confirmed sample of Sesar et al. (2010) (upper right-hand panel) and an eclipsing binary candidate with only slightly different minima and near-sinusoidal light variation (bottom right-hand panel). This eclipsing binary, when folded by half of the period, shows a folded light curve very similar to that of an RRc variable, as the tiny difference in the depths of the minima is masked by the error bars. If, in addition, such eclipsing binaries fall close to the colour–colour region of RRc stars, then automated classification will be difficult. However, the PC1 spectrum

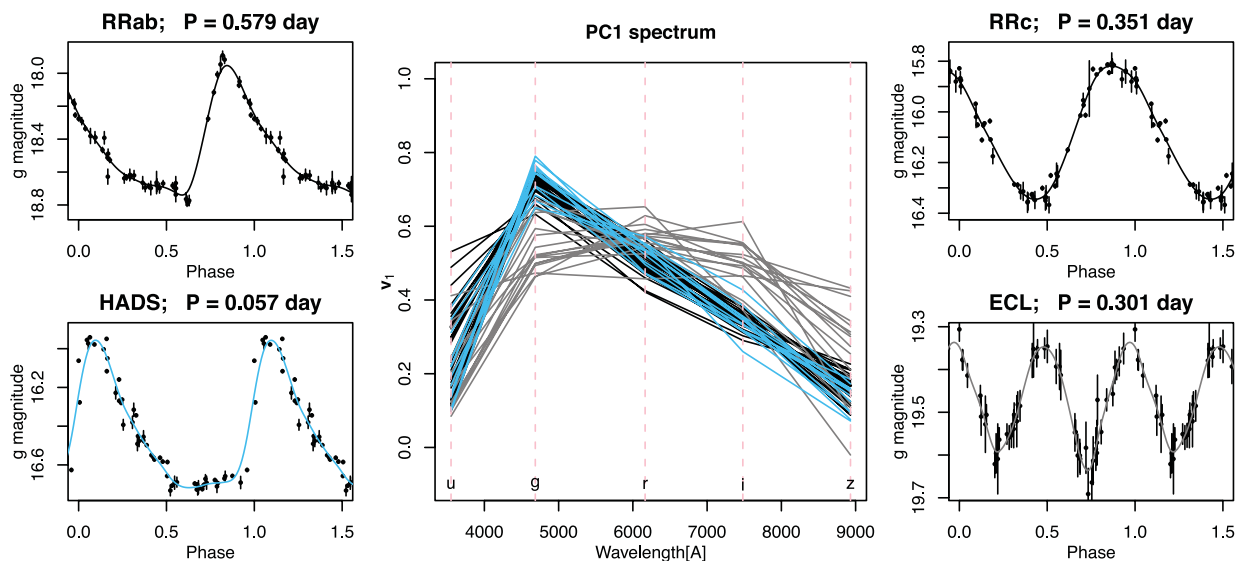


**Figure 6.** Examples of folded light curves (top left-hand panel: RRab; bottom left-hand panel: HADS; top right-hand panel: RRc; bottom right-hand panel: eclipsing binary) and some PC1 spectra ( $v_1$ ) of the classes RR Lyrae (black lines), HADS (blue) and eclipsing binary (grey). There is a marked difference between the two pulsating types and the eclipsing binaries.



is approximately flat-topped for these stars, whereas it has a peak at  $g$  for a pulsating RRc. The inclusion of the first principal direction  $v_1$  can thus be helpful in an automated classification procedure.

## 4.2 Random Forest classification

### 4.2.1 Preliminary selection

As our goal is to extract only a few variable types of interest from the SDSS Stripe 82 sample, we define our classes as RRAB, RRC, HADS and O, corresponding to the four types RRab, RRc, HADS and ‘other’, respectively. Supervised classification needs a set of objects with known types and well-measured attributes to train the classifier. For RRab- and RRc-type variables, the sample of Sesar et al. (2010) provides such a set. For HADS stars, we do not have a confirmed data base. However, they form a relatively well defined, separable class of variable stars, so we can select visually a sample of plausible HADS candidates for the training set. Class O, on the other hand, is broad enough to elude all concise, easy-to-implement definition. Our only requirement can be precisely this broadness: class O in the training set should contain representatives of all alternative types of variables mixed together, except for RR Lyrae or HADS stars. A reasonable criterion is therefore the separability of this class from HADS, RRAB and RRC. Thus, to obtain a clean training set, we apply Random Forest classification on the visually selected sample, then we remove all HADS and O objects that were misclassified, and then we iterate these steps, until we reach a sample in which these two classes are recognized cleanly. As the RRAB and RRC classes are already confirmed, we removed only the O objects that were classified as RRAB or RRC, but not the RRAB and RRC stars that were misclassified as O.

For the visual selection of the HADS training sample, we have expressed all possible selection criteria in the framework of PCA. The extraction of variable objects was performed with the aid of the variance proportion of the first principal component. To reflect the astrophysical properties of the sought stars, we also require them to show the characteristic colour changes during the cycle. In the language of PCA, this corresponds to have broadly the PC1 spectrum demonstrated by the blue lines in the middle panel of Fig. 6. Furthermore, they must have admissible  $u - g$  and  $g - r$  colours. Also, the dominant frequency  $F_{z_1}$  of the time-series of the first principal component  $z_1$  must correspond to the HADS frequency range. In summary, the selection criteria are as follows:

- (i) PC1 has a variance proportion higher than the 0.9999 quantile of that of a five-variate standard normal point cloud with the same number of observations.
- (ii) The PC1 spectrum  $v_1 = (v_{u1}, v_{g1}, v_{r1}, v_{i1}, v_{z1})^T$  satisfies the following cuts:  $0 < v_{u1} < 0.8$ ,  $0.45 < v_{g1} \leq 1$ ,  $0.3 < v_{r1} < 0.75$ ,  $0.15 < v_{i1} < 0.6$ ,  $0 < v_{z1} < 0.5$ .
- (iii) The (extinction-corrected) median colours are in the region  $0.7 < u - g < 1.4$  and  $-0.2 < g - r < 0.4$  of the  $u - g$ ,  $g - r$  diagram.
- (iv)  $F_{z_1} > 3 \text{ d}^{-1}$ .

All cuts are given very broadly, so the resulting selection contains a majority of contaminating objects such as eclipsing binaries with flat PC1 spectra, quasars, main-sequence variables and even RRC stars. Visual inspection of the  $g$ -band light curves resulted in 117 plausible HADS candidates. The training set for the first cleaning iteration consisted of these as class HADS, the RRab and RRC variables of Sesar et al. (2010) as classes RRAB (379 objects) and RRC (104 objects), respectively, and a random selection of

2400 other (O) variables from the remaining variable set, yielding a training set of 3000 objects in total. For all objects we calculated the following attribute list:

- (i) The median (apparent) magnitudes in all bands, corrected for interstellar extinction using the dust map of Schlegel, Finkbeiner & Davis (1998);
- (ii) The median (extinction-corrected) colours  $u - g$ ,  $g - r$ ,  $r - i$  and  $i - z$ ;
- (iii) The interquartile range  $\text{IQR}_u = q_u(0.75) - q_u(0.25)$ , ... of every band and of the first principal component scores  $z_{11}, \dots, z_{1T}$  as a percentile-based estimate of the light-curve range, where  $q_x(p)$  denotes the empirical  $p$  quantile of the time-series  $x$  ( $x = u, g, r, i, z$  and PC1);
- (iv) Percentile estimate  $S_u = [q_u(0.9) + q_u(0.1) - q_u(0.5)] [q_u(0.9) - q_u(0.1)]^{-1}$ , ... of the light-curve skewness for all bands, in addition to that of the first principal component scores;
- (v) The PC1 spectrum  $v_1 = (v_{u1}, v_{g1}, v_{r1}, v_{i1}, v_{z1})^T$ ;
- (vi) The dominant frequency  $F_{z_1}$  found by the period search method described in Section 3.2.

The median apparent magnitudes were included to help the classifier to account for the distance-dependent shape of the PC1 spectrum. Selection of a small but sufficient attribute set is nevertheless necessary: the performance of most data mining procedures is sensitive to the presence of noise-like attributes. The importance of any attribute can be measured by Random Forest by, for example, calculating the average accuracy loss on trees generated without the use of the attribute in question. If the accuracy loss is high, then the attribute is very important. The plot of loss for all attributes in Fig. 7 indicates that the best two attributes are the frequency and the  $g$ -band component  $v_{g1}$  of the first principal direction. They are followed by the  $r - i$  and  $g - r$  median colours, then another two PCA-based attributes,  $v_{i1}$  and the IQR of the  $z_1$  time-series. The latter proves to be more important than the  $g$ -band IQR. The relatively low accuracy loss due to omission of colours is a consequence of our preselection of colour range in the  $u - g$ ,  $g - r$  plane and of the correlation between colours. The median apparent magnitudes did not prove to be useful, because the training set covered the complete range of occurring distortions of the PC1 spectrum, and was thus able to directly model the distortions of the PC1 spectrum. According to a procedure similar to that applied in sections 4.2–4.4 of Dubath et al. (2011), the most performant attribute set is the 11 top-ranking attributes:  $F_{z_1}$ ,  $v_{g1}$ ,  $r - i$ ,  $g - r$ ,  $v_{i1}$ ,  $\text{IQR}_{z_1}$ ,  $u - g$ ,  $S_g$ ,  $i - z$ ,  $S_{z_1}$  and  $\text{IQR}_g$ . This is what we used for the following cleaning of the training set and the extraction of our set of candidate RR Lyrae and HADS stars.

The next stage is the cleaning of the training set, to obtain clearly separated HADS and O classes. In the first iterative step of this, Random Forest was trained on the 3000 objects using the attribute list presented above. At this stage, the set O may contain unrecognized RR Lyrae and HADS stars. We assume that this contamination is low enough not to bias strongly the automated classification results for class O in the first run, as these are relatively rare compared to all other types taken together. An overall error rate less than 1 per cent in the first iteration confirmed this assumption. After each run of Random Forest, we removed the objects from types O and HADS that were misclassified (keeping all RR Lyrae stars regardless of the predicted type, since these are confirmed variables), and repeated classification. After three iterations, we ended up with 108 HADS and 2372 O stars, which were separated perfectly from each other and from the RR Lyrae classes. The only confusion arose from 10 RRAB and RRC stars that were classified as type O, and one RRAB

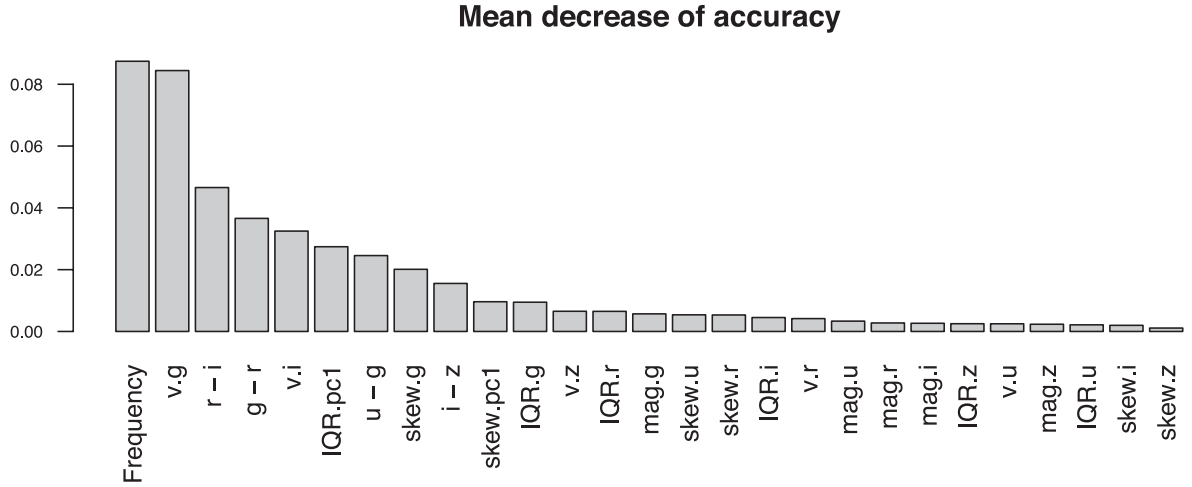


**Figure 7.** Attribute ranking by mean accuracy decreases when classifying without the attribute in question. The components  $v_{1g}$  and  $v_{1i}$  of the PC1 spectrum are highly ranked, comparable to the frequency,  $r - i$  and  $g - r$  colours.

**Table 1.** RR Lyrae candidates in Stripe 82. ID: object identifier; RA: right ascension ( $^{\circ}$ ); Dec.: declination ( $^{\circ}$ ); Type: subtype (RRab or RRC);  $u_{\text{med}}$ ,  $\dots$ : median magnitudes corrected for the interstellar medium extinction;  $F_{z_1}$ : pulsation frequency determined from generalized least-squares period search on PC1;  $A_u$ ,  $\dots$ : amplitudes from a B-spline fit to the folded light curves. The complete table is available online.

ID	RA	Dec.	Type	$u_{\text{med}}$	$g_{\text{med}}$	$r_{\text{med}}$	$i_{\text{med}}$	$z_{\text{med}}$	$F_{z_1}$	$A_u$	$A_g$	$A_r$	$A_i$	$A_z$
510582	−11.901668	−0.947130	RRAB	20.22	19.14	18.90	18.79	18.79	1.24630	0.20	0.19	0.13	0.11	0.09
651051	19.017164	1.262702	RRAB	18.27	17.07	16.80	16.72	16.69	1.77625	1.03	1.09	0.76	0.62	0.56
1013845	23.603725	−0.592160	RRAB	17.32	16.11	15.87	15.77	15.77	1.36722	0.83	0.88	0.62	0.53	0.44
1918041	−31.227027	−0.703085	RRC	20.83	19.69	19.62	19.61	19.69	2.65171	0.39	0.44	0.28	0.18	0.25
2654711	−41.834262	−0.994213	RRC	17.66	16.48	16.54	16.62	16.69	4.88670	0.19	0.22	0.16	0.12	0.11
2725572	−40.845223	−0.719055	RRAB	20.15	19.03	18.74	18.69	18.69	1.77540	1.25	1.09	0.75	0.60	0.36
3352291	−46.471817	1.260386	RRAB	15.85	14.67	14.41	14.33	14.34	1.95774	1.30	1.32	0.93	0.77	0.66
$\vdots$														

classified as RRC. This procedure biases the subsequent extraction of HADS towards purity against completeness, as we dropped all cases that might represent unusual specimens of classes, and the final selection does not fully take into account eventual real similarities between stars belonging to distinct types. The choice between purity and completeness is certainly subjective, and depends on the purpose of the study.

Re-processing the variables corresponding to criterion (i) above by Random Forest using the resulting training set gave 317 candidates, 163 HADS, 82 RRC and 72 RRAB stars. Multifrequency analysis as presented in Section 3.2 was performed on them. The final visual check was done with the help of ‘portraits’ of the stars: summary plots (Figs A1–A7) that contained the most important information that could have been extracted from the data, namely  $z_1$  and residual frequency spectra, folded  $z_1$ ,  $g$ ,  $g - i$  and residual light curves, the raw observed time-series, colour–colour, colour–period and period–amplitude diagrams, and the PC1 spectrum. These plots are described and presented for a few stars in Appendix A, and are available for the complete final sample as online material (see the Supporting Information). For many of the stars, the frequency spectrum has a noisy and complex aspect, often burdened with strong aliases, the presence of several secondary peaks, and a strongly asymmetric appearance of the spectral window. During the visual selection, we accepted several candidates with a low-significance periodogram peak if they had a clear folded light curve, they showed strong periodic colour variations and the characteristic PC1 spectrum, and they were situated in the correct region of the colour–

colour diagram. In one case (object 2722220), the extremely low number of observations and the resulting low-significance peak point to a HADS frequency, which is erroneous, though the folded light curve is very clean; the object otherwise shows all the required characteristics for a HADS, and is situated in the overlap of the HADS and RR region of the colour–colour diagram. This object was detected in ASAS as an RR Lyrae (Szczygiel & Fabrycky 2007). In a few other cases, though the average noise level is not particularly high, there are groups of other peaks with comparable heights in the periodogram. Stars with unclear periodogram and less certain frequency identification are denoted by an asterisk beside their object identifier in Tables 1 and 6; their summary figures can be consulted as online material (see the Supporting Information). The visually selected 132 HADS, 68 RRab, 36 RRC and 25 multi-periodic or peculiar RR Lyrae candidates are discussed in the next two sections.

#### 4.2.2 Candidate RR Lyrae variables

The list of the 68 RRab-type and 36 RRC-type objects is given in Table 1, containing the identifier, coordinates, median magnitudes corrected for interstellar extinction, the frequency and the bandwise amplitude estimates derived from a B-spline fit to the folded light curve. A summary plot for one of them is presented in Fig. A1. For the ease of eventual further analysis and in order to present our addition to the sample of Sesar et al. (2010) in a coherent way, we fitted this new set of stars with the templates published there, and

**Table 2.** Best-fitting templates of Sesar et al. (2010) for the new RR Lyrae candidates in Stripe 82. ID: object identifier; RA: right ascension (°); Dec.: declination (°);  $d$ : heliocentric distance for stars included in Fig. 9;  $\langle V \rangle$ : mean dereddened  $V$ -band magnitude, determined from a best-fitting  $V$ -band template synthesized from the best-fitting  $g$  and  $r$  templates,  $A'_u, \dots$ : amplitudes;  $\phi_0^u$ : epoch of maximum brightness;  $u_0$ : the magnitude at the epoch of maximum brightness corrected for the interstellar medium extinction (the last three determined from the best-fitting template);  $T_u, \dots$ : best-fitting template identifier number as given in Sesar et al. (2010). The asterisks indicate slightly underestimated values.  $d$  and  $\langle V \rangle$  were computed only for those RRab variables that are plotted on Fig. 9, and are therefore missing for some stars. The complete table is available online.

ID	RA	Dec.	$d$	$\langle V \rangle$	Period	$A'_u$	$\phi_0^u$	$u_0$	$T_u$	$A'_g$	...
510582	−11.901668	−0.947130			0.802373	0.194	54358.25	20.113	104	0.187	...
651051	19.017164	1.262702	17.256	16.785	0.562973	0.604*	53639.39	17.766	100	0.663*	...
1013845	23.603725	−0.592160	11.322	15.870	0.731397	0.687*	54029.29	16.816	101	0.659*	...
1918041	−31.227027	−0.703085			0.377115	0.375	54012.05	20.612	0	0.416	...
2654711	−41.834262	−0.994213			0.204637	0.161	53675.09	17.567	0	0.167	...
2725572	319.154777	−0.719055	42.543	18.744	0.563272	0.626	53625.21	19.650	102	0.666*	...
3352291	313.528183	1.260386	5.600	14.341	0.510786	0.559*	53704.09	15.349	100	0.598*	...
⋮											

listed the template amplitude, the epoch of maximum brightness, the magnitude at the epoch of maximum brightness and the identifier of the best template in Table 2. There were several RRab stars that did not have acceptable template fits for all or part of the bands, as the template set is not all-encompassing (see fig. 7 in Sesar et al. 2010). Such light curves showed a sharper rising branch, a narrower peak and a decreasing branch composed of a steep initial fading from the brightest state and a more prolonged near-minimum state than the templates. One example, the same star that is presented in Fig. A1, is shown in Fig. 8. The template amplitudes of these stars are underestimated on average by around 10 per cent (up to 20 per cent); such cases are denoted in Table 2 by an asterisk following the amplitude value.

To form an overview about the new RR Lyrae sample, we investigated their spatial and period–amplitude distribution. For the RRab stars, we estimated the heliocentric distance following section 4.1.1 of Sesar et al. (2010). We assumed the same average halo metallicity of  $[\text{Fe}/\text{H}] = -1.5$  and a mean value  $M_V = 0.6$  for their absolute magnitude. The extended heliocentric map of the halo is presented in the left-hand panel of Fig. 9. The new variables form part of the already known structures (Watkins et al. 2009; Sesar et al. 2010),

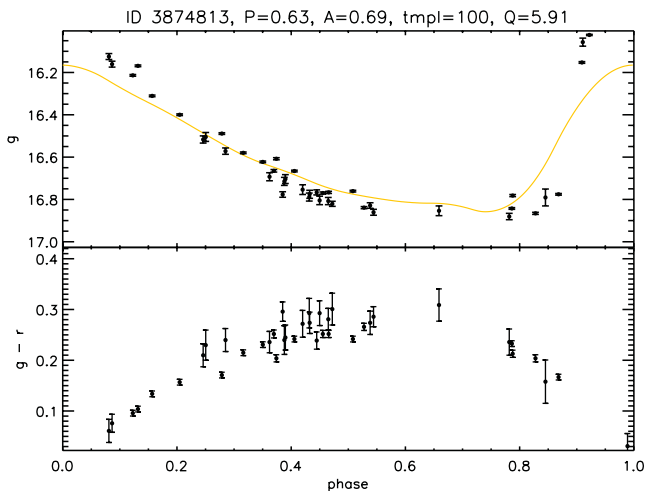


**Figure 8.**  $g$ -band template fit for star 3874813, using the templates of Sesar et al. (2010), an example that cannot be fitted well by these. For comparison, see the second panel from the top in the middle column of Fig. A1, which shows the same star fitted with a B spline.

in the majority of the Hercules–Aquila Cloud. The middle panel of Fig. 9 shows their period–amplitude diagram, using an amplitude estimate derived from B-spline fitting of the individual  $g$ -band light curves. For comparison with the confirmed RRab sample, we plot the quadratic relationship

$$A_g = -3.18 - 26.53 \log(\text{period}) - 37.88[\log(\text{period})]^2, \quad (2)$$

fitted to the Oosterhoff I type RRab stars with the best-quality light curves in the sample of Sesar et al. (2010) (their equation 21, solid line). The new RRab candidates are loosely aligned along this line, so the majority can be associated with Oosterhoff type I. As in their sample, we see a hint at a longer tail towards longer periods, but there is no clear bimodality, as in, for example, Miceli et al. (2008). This is confirmed by the histogram and the density estimate of the  $\log(\text{period})$  distances of the observed periods from the solid line. The distribution of the new candidates seems to be slightly shifted downwards with respect to the locus of the Oosterhoff I type stars. The shift may be explained by differences in the analysis. Sesar et al. (2010) use template amplitudes, which removes part of the statistical uncertainty, and gives more reliable amplitude estimates, if the templates indeed cover the variety of the light curves. However, the template set is insufficient. This requires direct estimates of amplitudes from the smoothed folded light curves for the new sample, and the resulting underfitting of the peaks can bias the amplitude estimates downwards. A more detailed comparison would require re-analysis of the complete Stripe 82 RRab sample and an extension of the template set of Sesar et al. (2010), which is beyond the scope of this paper.

The multifrequency analysis, performed on all candidates with sufficient residual degrees of freedom, yielded 23 further objects with multiple modes whose significance was confirmed by a combination of bootstrap and extreme-value procedures (though two with only very few residual degrees of freedom after smoothing), and two more showing clear light-curve changes without any indication of a second frequency. These are listed in Tables 3, 4 and 5.

Table 3 contains the found double-mode RR Lyrae candidates showing the theoretically expected fundamental-to-overtone frequency ratio close to 0.745 (12 stars, around 2 per cent of the total Stripe 82 RR Lyrae sample found in Sesar et al. 2010 and here). In addition, Table 3 lists two more objects for which the period search gave probably aliased results, and therefore the ratio is off for the frequencies corresponding to the maximum of the

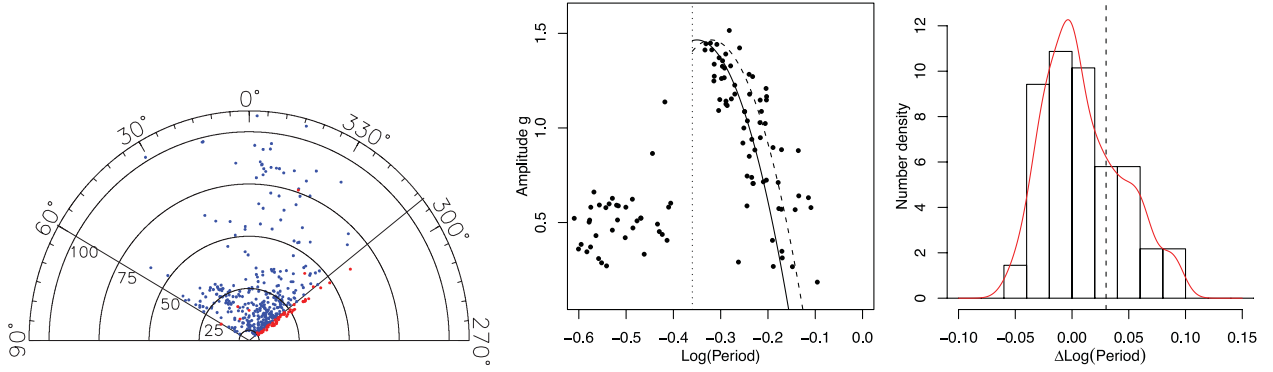


**Figure 9.** Left-hand panel: heliocentric map of the Stripe 82 RRab stars, based on the average halo metallicity value. The radial axis is the heliocentric distance in kpc and the angle is the equatorial RA. Blue dots: the sample of Sesar et al. (2010); red dots: the new candidate RRab stars. Middle panel:  $\log(\text{period})$ - $g$ -amplitude diagram of the RR Lyrae candidate sample. The solid line shows the position of likely Oosterhoff I type RRab stars and the dashed line denotes a plausible separation between Oosterhoff I and II types from Sesar et al. (2010). Right-hand panel: the distribution of the difference  $\Delta\log(\text{period})$  between the observed  $\log(\text{period})$  of the new RRab candidates and the value predicted by the quadratic relationship based on their amplitude.

**Table 3.** Double-mode RR Lyrae candidates in Stripe 82. Notation is the same as for Table 1.  $F_r$ : secondary frequency, Ratio: ratio of fundamental to first-overtone frequency,  $P_r$ :  $P$  value of secondary frequency.

ID	RA	Dec.	$u_{\text{med}}$	$g_{\text{med}}$	$r_{\text{med}}$	$i_{\text{med}}$	$z_{\text{med}}$	$F_{z1}$	$F_r$	Ratio	$P_r$	$A_u$	$A_g$	$A_r$	$A_i$	$A_z$
1059995	-23.605640	-0.056749	21.02	19.94	19.75	19.75	19.78	2.48876	1.85620	0.74583	0.000	0.19	0.36	0.27	0.22	0.09
1346981	25.772163	1.097024	18.20	17.09	17.03	17.03	17.04	2.82707	2.10280	0.74381	0.000	0.40	0.43	0.31	0.23	0.20
1638185	30.812051	1.205761	18.05	16.93	16.80	16.80	16.80	2.84693	2.11660	0.74347	0.000	0.48	0.49	0.37	0.31	0.24
1875049	-30.900196	0.941754	19.66	18.57	18.50	18.48	18.48	2.41850	1.80320	0.74558	0.000	0.20	0.35	0.24	0.19	0.22
2249641	-39.804740	0.210125	17.47	16.38	16.31	16.32	16.34	2.78830	2.07536	0.74431	0.000	0.45	0.48	0.33	0.26	0.22
2662389	-44.787449	0.404872	18.22	17.13	17.06	17.08	17.11	2.84001	2.10780	0.74218	0.000	0.38	0.44	0.30	0.24	0.21
2740388	-44.211467	-1.202920	17.61	16.54	16.47	16.45	16.50	2.76911	2.06080	0.74421	0.000	0.45	0.49	0.34	0.28	0.21
3091639	48.387957	0.715216	19.33	18.24	18.14	18.16	18.19	2.82369	2.09916	0.74341	0.000	0.44	0.55	0.36	0.29	0.23
3182847	-48.344716	0.330749	20.53	19.42	19.33	19.36	19.40	2.77071	2.06144	0.74401	0.000	0.38	0.50	0.39	0.28	0.29
3524879	-49.385512	-0.480494	17.52	16.37	16.28	16.27	16.29	2.42901	1.81232	0.74612	0.000	0.39	0.47	0.32	0.26	0.21
4185977	-52.885267	-0.892139	15.96	14.84	14.71	14.70	14.75	2.64865	1.97572	0.74593	0.000	0.48	0.53	0.38	0.30	0.26
5631911	-57.845165	-0.839656	19.85	18.74	18.66	18.57	18.63	2.43680	1.81908	0.74650	0.000	0.49	0.51	0.34	0.27	0.26
1149344	-21.758206	0.077395	20.22	19.16	19.03	18.99	18.99	2.40371	2.79388	0.86035	0.000	0.32	0.37	0.25	0.18	0.18
1283137	27.742275	-0.847584	19.08	17.92	17.83	17.82	17.84	1.75063	2.04704	0.85520	0.000	0.40	0.48	0.32	0.24	0.22

**Table 4.** RR Lyrae candidates with closely spaced multiple frequencies or indicating period, phase or amplitude shifts in Stripe 82. Notation is the same as for Table 3.

ID	RA	Dec.	$u_{\text{med}}$	$g_{\text{med}}$	$r_{\text{med}}$	$i_{\text{med}}$	$z_{\text{med}}$	$F_{z1}$	$F_r$	Ratio	$P_r$	$A_u$	$A_g$	$A_r$	$A_i$	$A_z$
1139404	-24.140121	0.369111	17.71	16.54	16.54	16.57	16.62	3.63296	3.62848	0.99877	0.000	0.33	0.38	0.28	0.21	0.18
1945634	-31.463604	1.030967	17.50	16.32	16.11	16.01	15.98	1.53242	1.53904	0.99570	0.035	0.52	0.58	0.37	0.27	0.26
2954798	-41.387218	-0.569949	18.15	16.95	16.97	17.01	17.06	3.15265	3.15188	0.99976	0.001	0.46	0.53	0.37	0.30	0.23
3261654	-45.603648	0.149636	17.01	15.81	15.83	15.87	15.93	3.68724	3.61116	0.97937	0.012	0.22	0.26	0.18	0.15	0.11
6058913	-58.281094	1.205592	18.29	17.13	17.06	17.08	17.12	2.55444	2.55320	0.99951	0.040	0.48	0.50	0.35	0.30	0.26
6086465	-57.509052	-0.506643	18.44	17.26	17.31	17.38	17.43	3.63835	3.71848	0.97845	0.010	0.31	0.32	0.25	0.21	0.22
700313	15.188040	-1.036745	17.85	16.72	16.56	16.50	16.51	2.99438			0.603	0.51	0.66	0.39	0.30	0.24
1731088	-30.677761	-0.062001	20.20	19.14	18.97	18.96	18.95	1.96133			0.357	0.87	0.91	0.66	0.51	0.49

**Table 5.** Multiperiodic RR Lyrae candidates with unusual period ratios in Stripe 82. Notation is the same as for Table 3.

ID	RA	Dec.	$u_{\text{med}}$	$g_{\text{med}}$	$r_{\text{med}}$	$i_{\text{med}}$	$z_{\text{med}}$	$F_{z1}$	$F_r$	Ratio	$P_r$	$A_u$	$A_g$	$A_r$	$A_i$	$A_z$
3218459	-47.774708	0.387032	17.23	16.10	16.13	16.20	16.27	4.48794	3.60676	0.80366	0.000	0.15	0.17	0.12	0.10	0.08
1528004	-29.845729	-0.438433	18.35	17.19	17.07	17.05	17.08	3.05227	5.03044	0.60676	0.020	0.87	0.92	0.67	0.53	0.46
3252839	-46.822139	-1.190310	17.83	16.69	16.70	16.75	16.80	3.21292	5.15024	0.62384	0.001	0.35	0.36	0.29	0.20	0.20



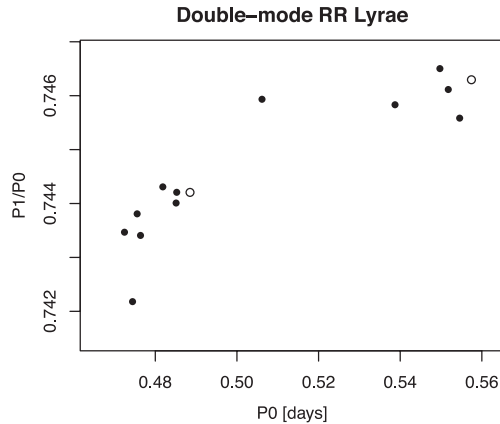


**Figure 10.** Petersen diagram for the candidate double-mode RR Lyrae variables. Black dots: candidates with well-identified frequency peaks; empty circles: aliased candidates, plotted here with the corrected periods.

periodogram. However, supposing another alias to be the true frequency ( $F_r - 1 \text{ d}^{-1}$  for the fundamental mode of object 1149344 and  $F_{z_1} + 1 \text{ d}^{-1}$  for the overtone in the case of object 1283137), the stars are in the regions admissible for double-mode RR Lyrae variables on the colour–colour, colour–period and period–amplitude diagrams. With these frequency choices, they also fit well the relationship between the fundamental period and the period ratio, as shown by the empty circles in Fig. 10. Of our list, seven are new, while the other seven were identified by Wils (2009). The summary information plot for one of them is presented in Fig. A2. The span of periods indicates a broad range of metallicities and/or masses to account adequately for the observed ranges of periods and ratios (see e.g. Alcock et al. 2000).

Table 4 contains RR Lyrae candidates with two closely separated frequencies and/or showing multiple thread structure in their folded light curves, together with two others showing multiple threads without the presence of a resolved second frequency (see the example given in Fig. A3). Such properties may be due to the Blazhko effect, slow periodic or irregular modulations of the amplitude or of the period. The folded-light-curve panels in Fig. A3 indicate the Julian Date of the observation with colours (the colour legend is given under the folded light curves), and the different threads visibly belong to different years of observations. For this object, the separation of the two frequencies is very small, suggesting possibly a long Blazhko period, the presence of period changes or phase shifts. We list two more objects (6058913 and 6086465) with very small number of data where the smoothing left very few residual de-

grees of freedom, but the bootstrap indicated presence of secondary modes. More observations of these objects are needed before their type can be resolved.

Several other RR Lyrae candidates showed two significant peaks at neither closely spaced nor fundamental-first overtone frequencies. Objects with similar frequency ratios were recently found by Soszyński et al. (2010) in OGLE data in the Large Magellanic Cloud and by Olech & Moskalik (2009) in  $\omega$  Centauri. We present three of them in Table 5 for which the Monte Carlo assessment showed these secondary peaks are significant. The first one, with its period ratio around 0.8, may be a candidate double-mode RR Lyrae star pulsating in the first and second overtone (its summary information plots are given in Appendix A, Fig. A4); the other two show period ratios around 0.6. These objects need further data for confirmation.

#### 4.2.3 HADS candidates

Using the training set described in Section 4.2.1, the Random Forest procedure selected 163 candidates. This was reduced by a subsequent visual inspection to 132 accepted HADS candidates, 111 monoperiodic and 22 possible multiperiodic stars. The complexity of the frequency spectra is even more pronounced in this class than among the RR Lyrae sample. Table 6 presents a summary of the basic properties of the monoperiodic sample, similarly to Table 1. Two stars, one with symmetric and one with asymmetric folded light curves, are presented in Figs A5 and A6. All frequencies given in Table 6 can be affected by aliasing, though this does not modify the classification of the stars: for the typical frequencies of the HADS stars, aliasing would hardly lead to RR Lyrae frequencies and to a consequent misclassification. Their observed frequency distribution, concentrated at relatively high frequencies (shown in Fig. 11), suggests that the dominant population is metal-poor SX Phoenicis type (see fig. 1 in McNamara 2000b). However, in the absence of spectroscopic information, a confirmed classification into Population I ( $\delta$  Scuti) and Population II (SX Phoenicis) objects is not possible. The right-hand panel of Fig. 11 exhibits a correlation between the frequencies of the monoperiodic candidates (except for three objects, 2722220, 5824679 and 5972418, for which the periodogram peak is very low) and their location on the  $(u - g)$ ,  $(g - r)$  diagram. The blue edge of the HADS region is dominated by high-frequency candidates, whereas lower-frequency stars are grouped towards the red edge.

In this sample, we also found several suspected multiperiodic objects. The significance of the secondary peaks was much lower in the candidate multiperiodic HADS sample than among the double-mode RR Lyrae stars, and for all the objects presented here, warrants

**Table 6.** HADS candidates in Stripe 82. Notation is the same as for Table 1. The complete table is available online.

ID	RA	Dec.	$u_{\text{med}}$	$g_{\text{med}}$	$r_{\text{med}}$	$i_{\text{med}}$	$z_{\text{med}}$	$F_{z_1}$	$A_u$	$A_g$	$A_r$	$A_i$	$A_z$
558620	−12.512990	−0.604203	20.50	19.42	19.46	19.50	19.56	23.22362	0.68	0.69	0.51	0.33	0.41
516958	−13.867340	0.412679	17.37	16.40	16.32	16.37	16.43	17.68620	0.59	0.76	0.54	0.41	0.34
825896	−16.982811	−0.869013	17.57	16.41	16.33	16.37	16.43	20.17531	0.19	0.18	0.14	0.11	0.08
800977	−18.396891	1.189213	18.21	17.21	17.17	17.20	17.26	19.90575	0.25	0.30	0.23	0.18	0.17
799691	−19.685526	−0.304110	20.58	19.63	19.61	19.65	19.67	19.11502	0.41	0.58	0.43	0.31	0.29
407172	−8.778812	−0.076337	20.63	19.67	19.64	19.71	19.79	26.77966	0.15	0.23	0.19	0.17	0.16
16959	0.818054	1.074244	20.52	19.41	19.45	19.51	19.49	16.82779	0.73	0.71	0.54	0.43	0.39
173268	10.194452	−0.987410	20.01	19.02	18.86	18.83	18.85	16.12342	0.23	0.28	0.16	0.11	0.10
187850	13.118868	−0.016244	20.79	19.78	19.70	19.75	19.79	19.19475	0.22	0.27	0.19	0.12	0.19
610306	17.691082	0.312217	20.60	19.59	19.57	19.63	19.69	19.46323	0.46	0.28	0.25	0.18	0.27
⋮													

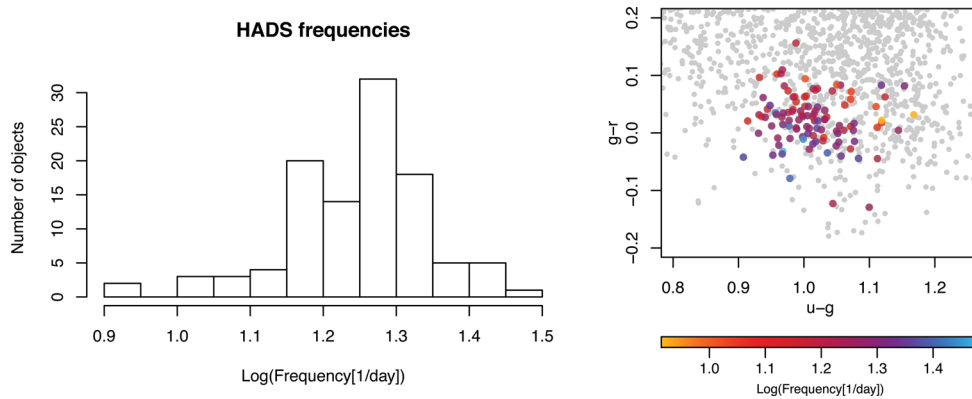


**Figure 11.** Frequency distribution (left-hand panel) and colour-colour diagram (right-hand panel) of the monoperoic HADS candidates. The multicolour dots correspond to the HADS candidates, their frequency coded by the colour shade of the dots. The code is given below the colour-colour diagram.

**Table 7.** Multiperiodic HADS stars in Stripe 82. Notation is the same as for Table 3.

ID	RA	Dec.	$u_{\text{med}}$	$g_{\text{med}}$	$r_{\text{med}}$	$i_{\text{med}}$	$z_{\text{med}}$	$F_{z_1}$	$F_r$	Ratio	$P_r$	$A_u$	$A_g$	$A_r$	$A_i$	$A_z$
4936224	58.031763	0.502842	17.71	16.81	16.81	16.85	16.94	17.91900	17.91776	0.99993	0.000	0.24	0.27	0.20	0.14	0.13
4433015	-51.994003	1.211038	19.39	18.37	18.34	18.36	18.38	15.86637	16.06300	0.98776	0.008	0.30	0.26	0.17	0.11	0.13
2816955	-44.450874	0.835961	16.95	15.95	15.97	16.06	16.14	25.80457	25.15836	0.97496	0.000	0.19	0.22	0.16	0.13	0.11
1113593	-20.457095	-0.775377	17.81	16.74	16.74	16.77	16.86	21.71685	21.04152	0.96890	0.000	0.23	0.29	0.21	0.17	0.14
1741727	-31.076033	-0.079779	20.06	19.01	18.95	18.99	19.05	20.68204	19.11928	0.92444	0.000	0.02	0.17	0.12	0.11	0.10
3642254	-47.102871	0.553778	17.37	16.30	16.33	16.40	16.47	21.67150	18.67376	0.86167	0.001	0.23	0.30	0.20	0.16	0.15
5401947	-55.894772	0.624779	16.67	15.60	15.62	15.67	15.78	11.90623	9.89844	0.83137	0.001	0.61	0.67	0.49	0.37	0.33
3269918	-45.136352	-1.230279	18.67	17.63	17.68	17.75	17.84	19.09286	24.45904	0.78061	0.000	0.46	0.49	0.37	0.28	0.24
2196466	-35.874290	-0.357666	19.32	18.30	18.19	18.19	18.23	9.31067	11.95100	0.77907	0.007	0.17	0.22	0.14	0.10	0.09
2777345	-42.763135	0.482715	17.94	16.93	16.83	16.84	16.90	18.57330	24.30612	0.76414	0.003	0.21	0.24	0.18	0.12	0.09
2383752	-37.431381	-0.842875	21.33	20.31	20.27	20.30	20.32	13.15213	9.90024	0.75275	0.009	0.25	0.40	0.27	0.20	0.18
5415273	-57.074003	-0.422064	18.34	17.30	17.25	17.30	17.35	14.23765	10.29948	0.72340	0.000	0.16	0.19	0.13	0.10	0.09
713584	-16.915188	0.737187	19.40	18.37	18.38	18.41	18.48	20.72999	20.92128	0.99086	0.015	0.21	0.26	0.19	0.15	0.12
2298258	-36.580453	0.002215	20.43	19.49	19.50	19.57	19.62	20.24135	19.23308	0.95019	0.044	0.39	0.49	0.36	0.29	0.24
421829	-12.173045	0.426865	20.79	19.78	19.84	19.94	20.05	23.13966	25.14084	0.92040	0.034	0.16	0.22	0.17	0.11	0.07
225151	10.458869	-0.877921	17.94	16.84	16.87	16.91	16.98	18.25562	22.35908	0.81647	0.015	0.45	0.52	0.37	0.30	0.25
4064319	5.074867	-0.590467	17.95	16.90	16.90	16.98	17.08	21.84638	28.84696	0.75732	0.029	0.42	0.56	0.41	0.32	0.26
4377712	-50.876368	-1.088706	18.20	17.19	17.10	17.13	17.21	18.08047	24.00952	0.75305	0.040	0.60	0.70	0.50	0.40	0.34
3466895	-46.531706	-0.295154	20.75	19.75	19.73	19.81	19.92	21.52095	29.40172	0.73196	0.024	0.15	0.28	0.17	0.13	0.07
635626	15.536793	-0.854048	21.04	20.14	20.01	19.99	19.99	18.50370	25.39660	0.72859	0.011	0.02	0.22	0.18	0.16	0.27
3482070	-47.757087	-1.185417	17.29	16.28	16.32	16.41	16.52	25.81594	16.93232	0.65589	0.029	0.14	0.16	0.16	0.09	0.06
2211584	-35.050797	0.696938	20.82	19.89	19.84	19.89	19.95	17.68536	27.28028	0.64828	0.028	0.31	0.25	0.17	0.20	0.02

more observations for confirmation. We included a star into our candidate multiperiodic set only if two conditions held: (i) the combined bootstrap and extreme-value methods furnished a  $P$  value smaller than 0.05 for the peak in the residual spectrum; and (ii) the visual check of the folded residual light curve showed perceptible systematic variation rather than several outliers grouped by the folding. The properties of these stars are summarized in Table 7. We divided the table into two parts, the top half containing 12 objects with residual peaks more significant than 0.01, and the bottom half another 10 with secondary peaks with  $P$  value between 0.01 and 0.05. Among our multiperiodic candidates, we observed a broad variety of ratios between the primary and the residual periods at various levels of significance: they range from around 0.65 to near-one. The scatter of these values suggests a wide variety of objects of diverging types and with large differences in their characteristics such as the evolutionary state, mass, metal content or rotation. The majority of the most significant secondary peaks seem to form close doublets with

the main frequency. Such behaviour is quite frequent among low-amplitude  $\delta$  Scuti and SX Phoenicis stars (see e.g. Breger & Bishof 2002; Mazur et al. 2003; Poretti 2003). However, aliasing makes it difficult to find the true frequency in both principal component and residual spectra, and the presence of a strong secondary peak may also be the consequence of a not sufficiently precise primary frequency identification due to the relatively scarce number of observations per time-series. A few stars of our sample exhibit signs of amplitude or phase/period changes, light-curve threads separated by observational year and showing a high dispersion of the peak values (the clearest example is 225151, shown in Fig. A7).

## 5 DISCUSSION

Multifilter observations comprise much information about the characteristics of the observed star through the colour variations. We tested robust PCA as a way to extract information

about these variations. We found that PCA produces several useful quantities: the proportion of the variance of the first principal component to the total variance, the time-series of the first principal component, a robust notion of outlyingness, and the direction of the first principal component.

We found that the proportion of PC1 variance to the total variance is a useful variability indicator. The PC1 spectrum can help detect cases when excess variance is due to underestimated errors, by having one dominant and four near-zero elements. The time-series of PC1 yields the best attainable signal-to-noise ratio. Also, weights for period search can be defined based on a robust notion of outlyingness. Simulations and a test on real data containing several known RR Lyrae stars confirmed that period search on the PC1 time-series with robust weights decreases the impact of aliasing on the results.

The direction of the largest variation in the five-dimensional point cloud, which is termed the PC1 spectrum, proved to be useful in classification. For our sought sample of radially pulsating variables between 6500 and 7500 K, combined with bandwise SDSS error patterns, this direction points towards the *g* band, with decreasing contribution from the *r*, *i*, *u* and *z* bands. It was used in the Random Forest classification procedure as a new attribute helping to separate pulsating variables from eclipsing binaries. The coefficients of the *g* and *i* bands ranked among the best five attributes, besides the period and the *r* – *i* and *g* – *r* colours.

The study produced 132 HADS, 68 RRab, 36 RRC and 25 multiperiodic or peculiar RR Lyrae variable stars. The RR Lyrae stars are new addition to the confirmed RR Lyrae list of Sesar et al. (2010). The vast majority of these new RR Lyrae stars were found in the regions not originally considered by Sesar et al. (2010). Only a few RRab stars were missed by their work in the range considered by that study ( $308^\circ < \text{RA} < 60^\circ$  and  $|\text{Dec.}| < 1.25$ ), making their sample about 99 per cent complete. In the freshly included region, the time-series contain relatively few points (a median of 25), and thus period identification is subject to larger uncertainties than in their study. Among the new multiperiodic RR Lyrae stars, there are 14 double-mode candidates, several others showing signs of the Blazhko effect, period or phase change, and we found candidates with unusual period ratios, of which one may be a double-mode star pulsating in the first and second overtone. Among the HADS candidates, the multiperiodicity seems to show a broad variety of ratios between periods. The HADS candidates, similarly to the multimode RR Lyrae stars, need eventual observational follow-up to clarify and confirm their type and pulsation modes.

This work yielded promising results about the utility of PCA, and opens the way to further improvements. Missing data reduce the number of observations in the time-series of the first principal component to the number of data in the most scarcely observed band. Thus, though signal-to-noise ratio improves with the application of PCA, the decrease in the number of observations in the time-series can imply worse performance of period search. Optimization of the period search performance can be achieved either by restricting the analysis to the combination of only the best bands or by a statistical methodology that is able to deal with the missing values. Further investigations will explore these interesting possibilities.

## ACKNOWLEDGMENTS

MS wishes to thank J. Jurešik and G. Kovács for helpful discussions, and the two referees for their constructive suggestions. The work was supported by the Swiss National Science Foundation MHV grant PMPDP2\_129178.

Funding for SDSS and SDSS-II has been provided by the Alfred P. Sloan Foundation, the Participating Institutions, the National Science Foundation, the US Department of Energy, the National Aeronautics and Space Administration, the Japanese Monbukagakusho, the Max Planck Society, and the Higher Education Funding Council for England. The SDSS website is <http://www.sdss.org/>.

SDSS is managed by the Astrophysical Research Consortium for the Participating Institutions. The Participating Institutions are the American Museum of Natural History, Astrophysical Institute Potsdam, University of Basel, University of Cambridge, Case Western Reserve University, University of Chicago, Drexel University, Fermilab, the Institute for Advanced Study, the Japan Participation Group, The Johns Hopkins University, the Joint Institute for Nuclear Astrophysics, the Kavli Institute for Particle Astrophysics and Cosmology, the Korean Scientist Group, the Chinese Academy of Sciences (LAMOST), Los Alamos National Laboratory, the Max Planck Institute for Astronomy (MPIA), the Max Planck Institute for Astrophysics (MPA), New Mexico State University, Ohio State University, University of Pittsburgh, University of Portsmouth, Princeton University, the United States Naval Observatory, and the University of Washington.

## REFERENCES

- Abazajian K. N. et al., 2004, *AJ*, 128, 502
- Abazajian K. N. et al., 2009, *ApJS*, 182, 543
- Alcock C. et al., 1997, *ApJ*, 486, 697
- Alcock C. et al., 2000, *ApJ*, 542, 257
- Aubourg E. et al., 1993, *The Messenger*, 72, 20
- Bramich D. M. et al., 2008, *MNRAS*, 386, 887
- Breger M., 1980, *ApJ*, 235, 153
- Breger M., Bischof K., 2002, *A&A*, 385, 537
- Breiman L., 2001, *Mach. Learn.*, 45, 5
- Chambers J., Cleveland W. S., Kleiner B., Tukey P., 1983, *Graphical Methods for Data Analysis*. Wadsworth International Group, Belmont, California
- Clement C. et al., 2001, *AJ*, 122, 2587
- Cleveland W. S., 1994, *The Elements of Graphing Data*. AT&T Bell Laboratories, Murray Hill, NJ
- Coles S. G., 2001, *An Introduction to Statistical Modelling of Extreme Values*. Springer-Verlag, London
- Davison A. C., Hinkley D. V., 2009, *Bootstrap Methods and their Application*. Cambridge Univ. Press, Cambridge
- Deb S., Singh H. P., 2009, *A&A*, 507, 1729
- Debosscher J., Sarro L. M., Aerts C. N., Cuypers J., Vandenbussche B., Garrido R., Solano E., 2007, *A&A*, 475, 1159
- Dubath P. et al., 2011, *MNRAS*, 414, 2602
- Everitt B. S., 2002, *The Cambridge Dictionary of Statistics*, 2nd edn. Cambridge Univ. Press, Cambridge
- Eyer L., Blake C., 2002, in Aerts C., Bedding T. R., Christensen-Dalgaard J., eds, *ASP Conf. Ser. Vol. 459, Radial and Nonradial Pulsations as Probes of Stellar Physics*. Astron. Soc. Pac., San Francisco, p. 160
- Eyer L., Blake C., 2005, *MNRAS*, 358, 30
- Frieman J. A. et al., 2008, *AJ*, 135, 335
- Hastie T., Tibshirani R., Friedman J., 2009, *The Elements of Statistical Learning: Data Mining, Inference and Prediction*, 2nd edn. Springer-Verlag, New York (available online at <http://www.stanford.edu/~hastie/pub.htm>)
- Ivezić Ž. et al., 2007, *AJ*, 134, 973
- Ivezić Ž. et al., 2011, preprint (arXiv:0805.2366)
- Jolliffe I., 2002, *Principal Component Analysis*, 2nd edn. Springer-Verlag, New York
- Kanbur S. M., Mariani H., 2004, *MNRAS*, 355, 1361
- McNamara D. H., 1995, *AJ*, 109, 1751
- McNamara D. H., 1997, *PASP*, 109, 1221

- McNamara D. H., 2000a, *PASP*, 112, 1096  
 McNamara D. H., 2000b, in Bregier M., Montgomery M., eds, *ASP Conf. Ser. Vol. 210, Delta Scuti and Related Stars*. Astron. Soc. Pac., San Francisco, p. 373  
 Mazur B., Krzemiński W., Thompson I. B., 2003, *MNRAS*, 340, 1205  
 Miceli A. et al., 2008, *ApJ*, 678, 865  
 Nemec J. M., Nemec A. F. L., Lutz T. E., 1994, *AJ*, 1108, 222  
 Olech A., Moskalik P., 2009, *A&A*, 494, L17  
 Palmer D. M., 2009, *ApJ*, 695, 496  
 Paltani S., Türler M., 2003, *ApJ*, 583, 659  
 Petersen J. O., Christensen-Dalgaard J., 1996, *A&A*, 312, 463  
 Pigulski A., Kolaczowski Z., Ramza T., Narwid A., 2006, *Mem. Soc. Astron. Ital.*, 77, 223  
 Pojmanski G., 2002, *Acta Astron.*, 52, 397  
 Pojmanski G., 2003, *Acta Astron.*, 53, 341  
 Poretti E., 2003, *A&A*, 409, 1031  
 R Development Core Team, 2010, *R: A Language and Environment for Statistical Computing*. R Foundation for Statistical Computing, Vienna, Austria. ISBN 3-900051-07-0, URL: <http://www.R-project.org>  
 Reimann J. D., 1994, PhD thesis, Univ. California, Berkeley  
 Richards J. W. et al., 2011, *ApJ*, 733, 10 (doi:10.1088/0004-637X/733/1/10)  
 Rimoldini L. et al., 2012, *MNRAS*, submitted  
 Rousseeuw P. J., 1985, *Math. Stat. Appl.*, 13, 283  
 Sarro L. M., Debosscher J., Aerts C., López M., 2009, *A&A*, 506, 535  
 Savanov I. S., Strassmeier K. G., 2008, *Astron. Nachr.*, 329, 364  
 Schlegel D. J., Finkbeiner D. P., Davis M., 1998, *ApJ*, 500, 525  
 Scranton R., Connolly A. J., Szalay A. S., Lupton R. H., Johnston D., Budavari T., Brinkman J., Fukugita M., 2005, preprint (arXiv:astro-ph/0508564v2)  
 Sesar B. et al., 2007, *AJ*, 134, 2236  
 Sesar B. et al., 2010, *ApJ*, 708, 717  
 Smith H. A., 1995, *RR Lyrae Stars*. Cambridge Univ. Press, Cambridge  
 Soszyński I. et al., 2009, *Acta Astron.*, 59, 1  
 Soszyński I., Udalski A., Szymanski M. K., Kubiak J., Pietrzynski G., Wyrzykowski L., Ulaczyk K., Poleski R., 2010, *Acta Astron.*, 60, 165  
 Spano M., Mowlavi N., Eyer L., Marquette J.-B., Burki G., 2011, *A&A*, 536, 60  
 Stetson P. B., 1996, *PASP*, 108, 851  
 Szczygiel D. M., Fabrycky D. C., 2007, *MNRAS*, 377, 1263  
 Tanvir N. R., Hendry M. A., Watkins A., Kanbur S. M., Berdnikov L. N., Ngeow C. C., 2005, *MNRAS*, 363, 749  
 Terrell D., Gross J., Cooney W. R., 2012, *AJ*, 143, 99  
 Udalski A., Kubiak M., Szymanski M., 1997, *Acta Astron.*, 47, 319  
 Watkins L. L. et al., 2009, *MNRAS*, 398, 1757  
 Wils P., 2009, *Inf. Bull. Var. Stars*, 5873, 1  
 Yoachim P., McCommas P., Dalcanton J. J., Williams B. F., 2009, *AJ*, 137, 4697  
 York D. G. et al., 2000, *AJ*, 120, 1579  
 Zechmeister M., Kürster M., 2009, *A&A*, 496, 577

## SUPPORTING INFORMATION

Additional Supporting Information may be found in the online version of this article.

**Table 1.** RR Lyrae candidates in Stripe 82.

**Table 2.** Best-fitting templates of Sesar et al. (2010) for the new RR Lyrae candidates in Stripe 82.

**Table 6.** HADS candidates in Stripe 82.

**Online figures.** Summary plots for the complete final sample.

Please note: Wiley-Blackwell are not responsible for the content or functionality of any supporting materials supplied by the authors. Any queries (other than missing material) should be directed to the corresponding author for the article.

## APPENDIX A: SUMMARY INFORMATION FIGURES FOR VISUAL CHECKS

These figures summarize the most important features of a star that can be derived from five-band photometric time-series.

The two plots on the top left-hand side contain the frequency spectrum of the time-series of  $z_{11}, \dots, z_{1T}$  and that of the residual PC1 time-series, with the found most significant frequencies in each emphasized by an orange line.

The three top panels in the middle column present the light curves of PC1 scores,  $g$  magnitudes and  $g - i$  colour folded with the main frequency, and the two top right-hand panels show the light curves of the PC1 and  $g$  residuals folded by the residual frequency. Spline smoothed lines are added to the PC1 and  $g$ -band light curves. The folded light curves are colour-coded according to the Julian date of the observation; this is particularly useful for detecting slow phase or amplitude changes. The colour code is given in a stripe under the residual light curves.

In the bottom row, we show the raw time-series of observations, the  $(u - g) - (g - r)$ ,  $(g - i) - \log_{10}(\text{period})$  and period–amplitude diagrams, and the PC1 spectrum. The raw time-series in the left-most bottom panel show the  $u$ ,  $g$ ,  $r$ ,  $i$  and  $z$  bands in blue, green, red, brown and black, respectively; time is given in Julian Dates. This panel is useful for detecting trends, shifts or eventual other deviations in the data that might cause problems in the period search. The second bottom panel is the  $(u - g) - (g - r)$  colour–colour diagram. The light-grey points here represent the general variable sample obtained by the condition imposed on the variance  $d_1^2$  of the first principal component and the cuts on the PC1 spectrum  $v_1$  (steps 1 and 2 of the preliminary selection procedure in Section 4.2.1). The black circles and dark-grey dots refer to the RRAb and the RRC sample of Sesar et al. (2010), respectively. The orange blob represents the candidate star. In the  $(g - i) - \log_{10}(\text{period})$  and the period–amplitude diagrams (third and fourth panels in the bottom row), the light-grey points represent only the candidate HADS and RR Lyrae variables (without distinction) that were selected by Random Forest. The black circles, dark-grey dots and orange blob have the same meaning as in the colour–colour diagram. For the amplitude–period diagram, we used the percentile-based estimate of the  $g$  light curve range as described in Section 4.2.1. The last plot, the PC1 spectrum, shows the  $v_1$  values of the object as an orange line versus the effective wavelengths (in Å) of the filters. The two grey lines here give the lower and the upper boundary of the band occupied by the 483 confirmed RR Lyrae stars of Sesar et al. (2010).



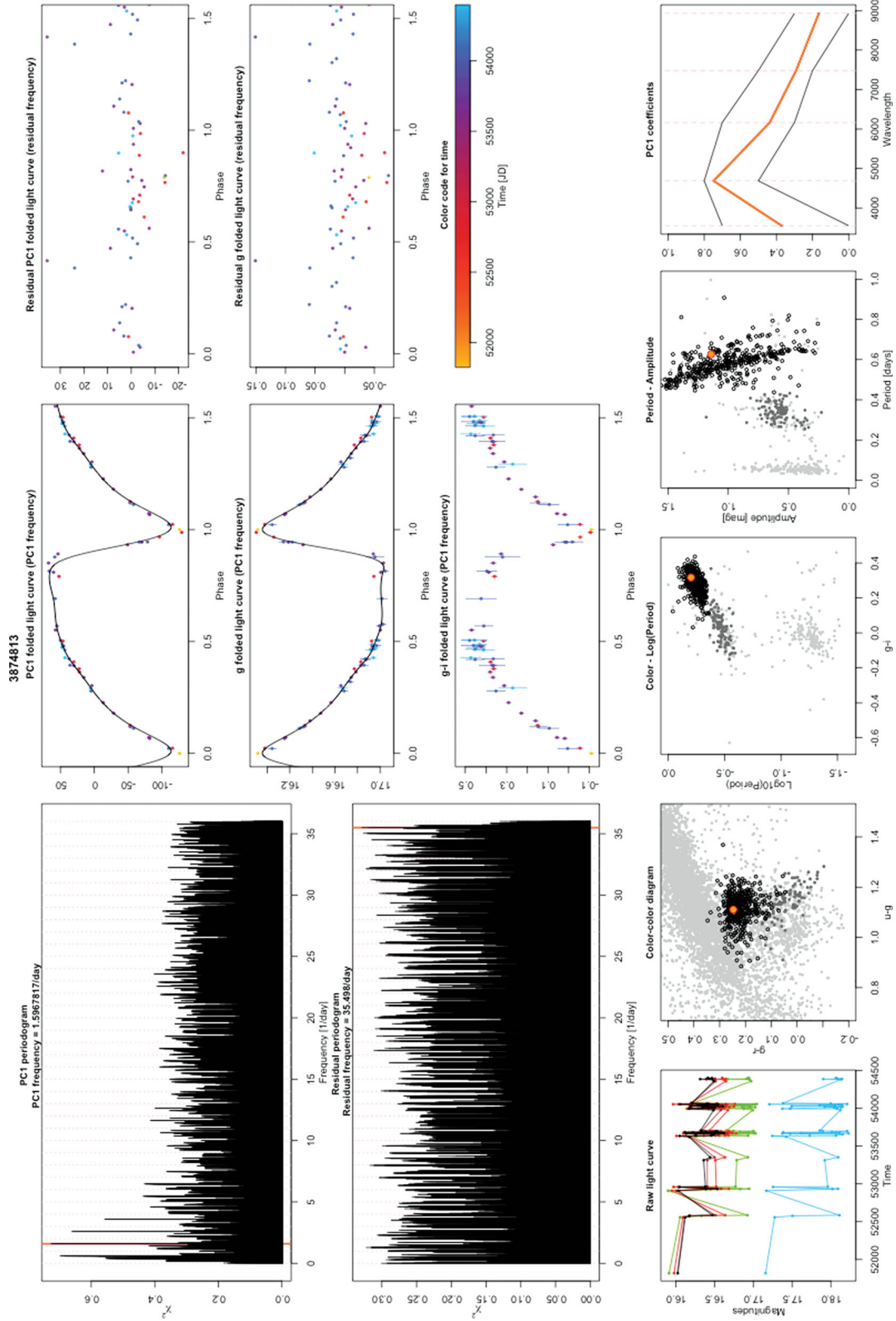
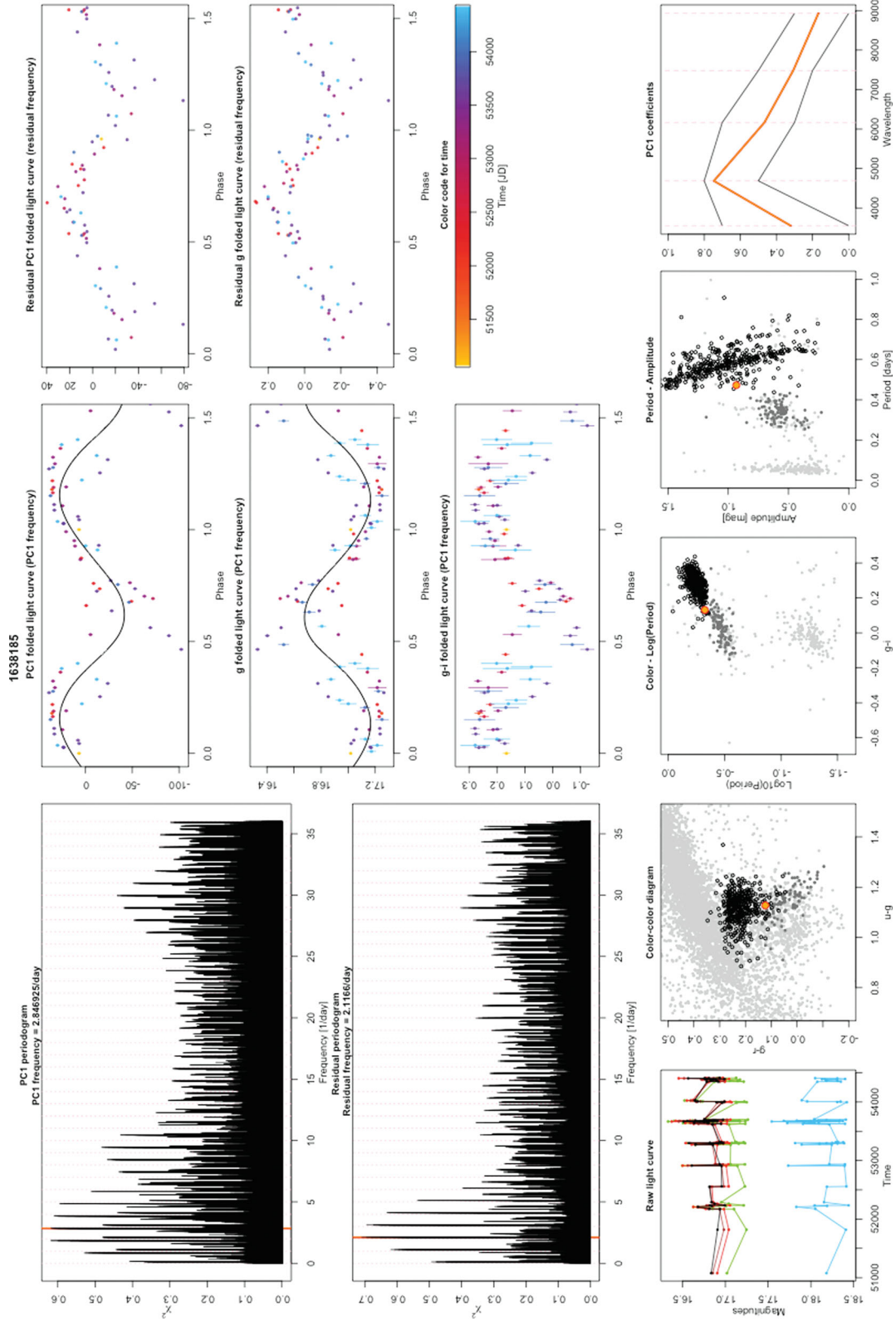
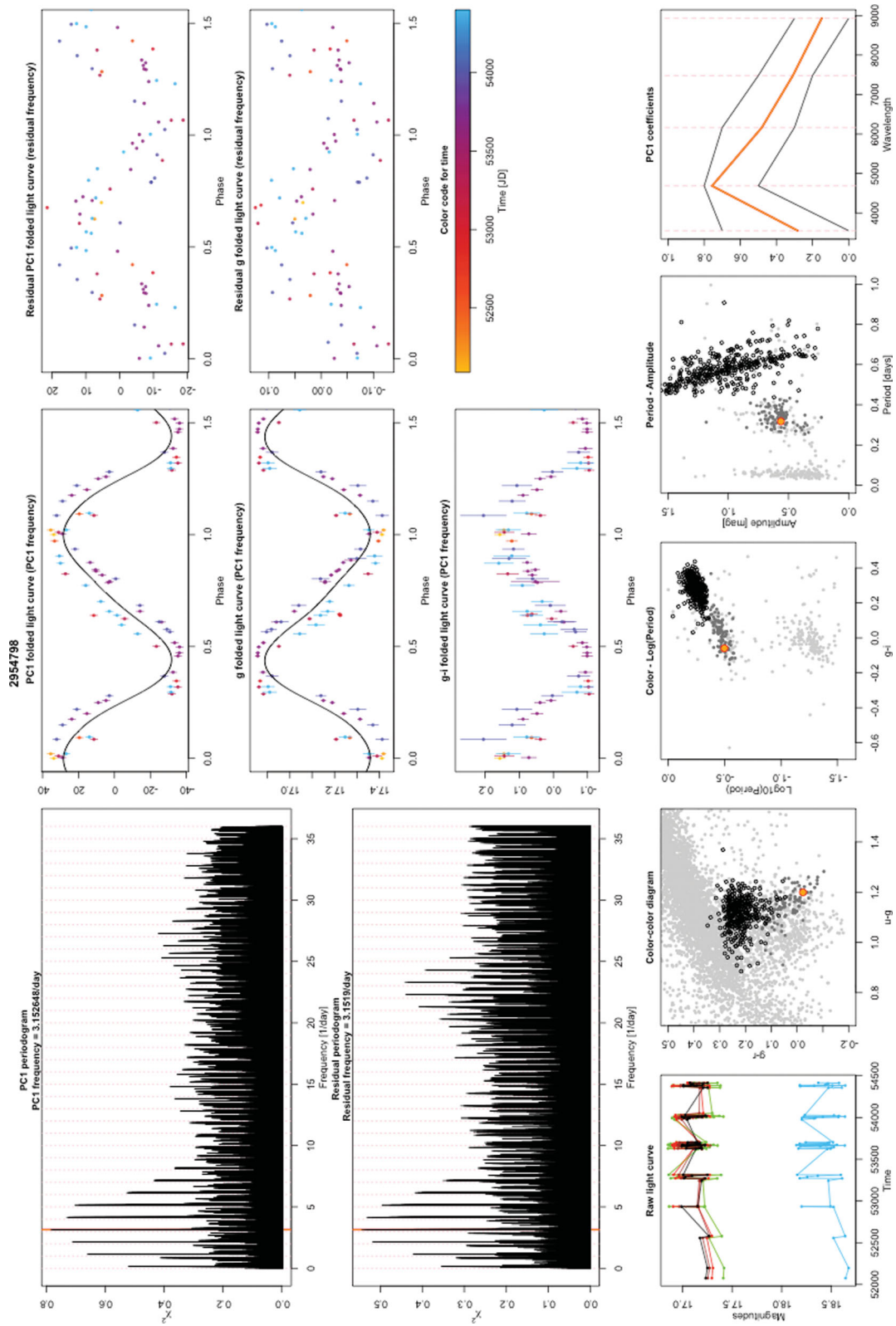


Figure A1. An RRab candidate. The legend is given in the text of the appendix.



**Figure A2.** A double-mode RR Lyrae candidate. The legend is given in the text of the appendix.



**Figure A3.** An RR Lyrae candidate showing signs of phase and amplitude shift and possible Blazhko behaviour. The legend is given in the text of the appendix.

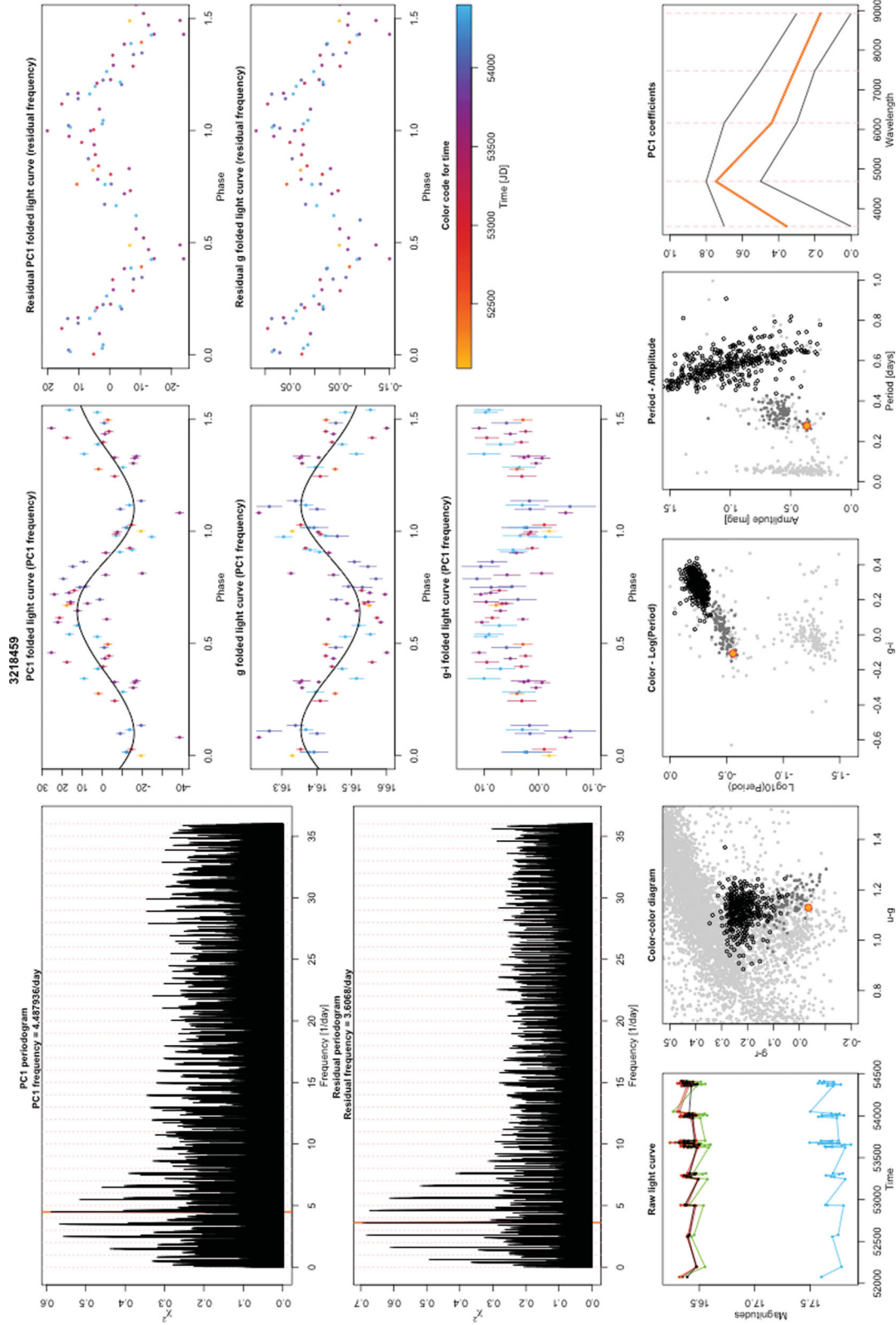
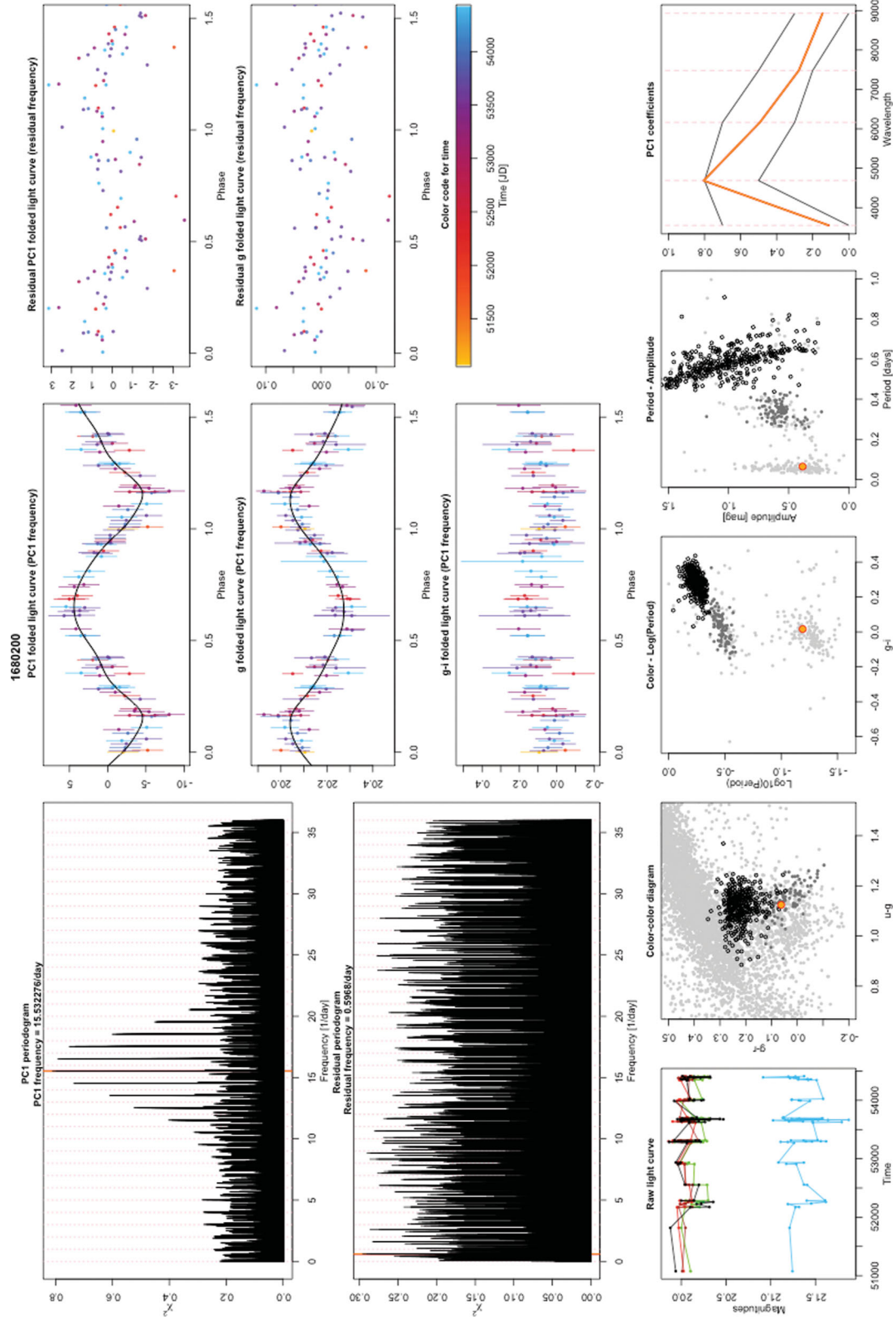


Figure A4. A double-mode RR Lyrae candidate, possibly pulsating in the first and second overtone. The legend is given in the text of the appendix.





**Figure A5.** A HADS candidate with symmetric light curves. The legend is given in the text of the appendix.

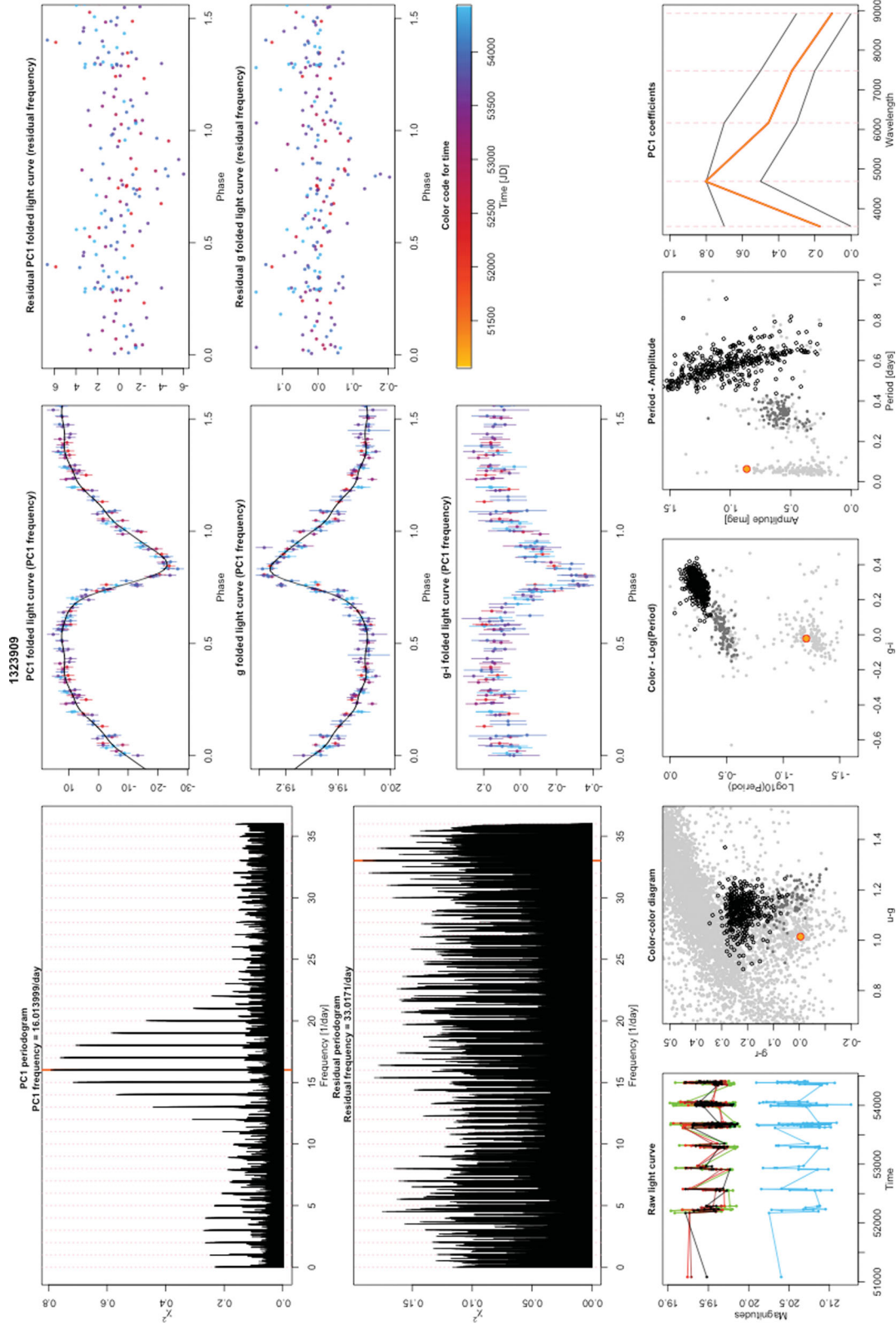
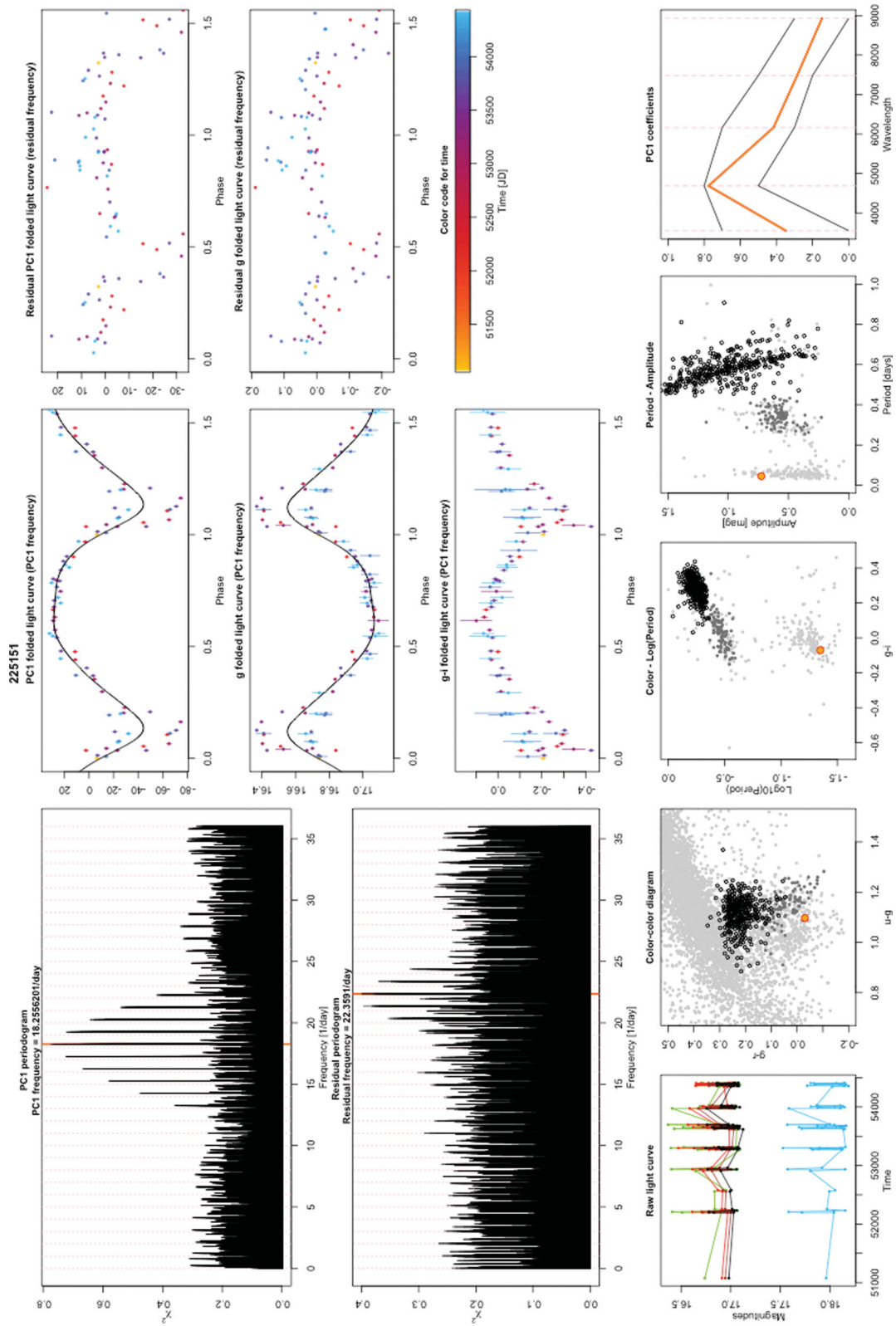


Figure A6. A HADS candidate with asymmetric light curves. The legend is given in the text of the appendix.



**Figure A7.** A double-mode HADS candidate with amplitude change indications. The legend is given in the text of the appendix.